ORNL/TM-2018/839

Computational Studies of Solid Stoppers for Generating Intense Exotic Radioactive Ion Beams at FRIB

Yuan Liu
Michael S. Smith
ORNL Physics Division

10/31/2018

OAK RIDGE NATIONAL LABORATORY
MANAGED BY UT-BATTELLE FOR THE US DEPARTMENT OF ENERGY

ORNL/TM-2018/839

Physics Division

Computational Studies of Solid Stoppers for Generating Intense Exotic Radioactive Ion Beams at FRIB

Yuan Liu
Michael S. Smith

Date Published: 10/31/18

Prepared by
OAK RIDGE NATIONAL LABORATORY
Oak Ridge, TN 37831-6354
managed by
UT-BATTELLE, LLC
for the
US DEPARTMENT OF ENERGY
under contract DE-AC05-00OR22725

CONTENTS

Page

LIST OF FIGURES

Page

LIST OF TABLES

Page

ABSTRACT

Low-emittance beams of rare isotopes at low energies (less than 3 MeV/u) are required for many high precision measurements in nuclear science research. Such beams will be produced at the Facility for Rare Isotope Beams (FRIB) by first slowing down and thermalizing or stopping fast fragmentation beams, and subsequently reaccelerating them to the required energies for experiments. The use of a solid stopper has the potential to provide high-intensity reaccelerated beams of many species. We performed simulations of the processes critical for generating beams in solid stoppers, including beam heating, external heating, diffusive release, effusive transport, and surface sticking. Using a variety of software tools, we investigated the viability of numerous solid stopper system designs for FRIB. We present our computational approach, the physical processes we modeled, the codes we used, and our results. We conclude with a proof-of-concept solid stopper system that releases ions sufficiently quickly for experiments with unstable reaccelerated beams at FRIB.

1. INTRODUCTION

Beams of radioactive nuclei are at the very frontier of nuclear science. They are needed for experiments to better understand the structure of nuclei, the cosmic origin of the elements, the nature of nuclear decay, and other fundamental interactions. These beams are also needed for a wide range of nuclear science applications including discovering new radionuclides for cancer diagnosis and treatment, detecting nuclear contraband at ports of entry, and assessing the safety of our nuclear stockpile.

The Facility for Rare Isotope Beams (FRIB) [1] is a next-generation radioactive ion beam (RIB) facility currently under construction at Michigan State University. Rare isotopes are produced at FRIB by the in-flight projectile fragmentation method, wherein a heavy ion beam (*e.g.*, Uranium) is accelerated to high energies to subsequently bombard a thin production target (*e.g.*, graphite). The beam-target interaction will create many high-energy, short-lived species via projectile fragmentation and in-flight fission. A system of magnets will separate out the rare isotopes of interest, some of which will be sent to target halls for use in experiments with these high energy (200 MeV/u) "fast" beams. However, beams of rare isotopes at lower energies (*e.g.*, less than 3 MeV/u) are required for many high precision measurements including nuclear mass measurements with Penning traps, laser spectroscopy, nuclear decay studies, and direct measurements of thermonuclear reactions that cause some stars to explode. Such low-energy beams will be produced at FRIB by first slowing down and thermalizing or stopping the fast beams, and subsequently reaccelerating them to the required energies for experiments. It is these low-energy reaccelerated beams that will make FRIB unique.

There are numerous challenges to production of the low-energy radioactive nuclear beams at FRIB. The most significant are in stopping the fast fragment beams and in transporting the stopped species for reacceleration. Three schemes have been proposed for stopping and transport: a cryogenic gas stopper [2], a cyclotron gas stopper [3], and a solid stopper system [4]. It is anticipated that all three schemes will be deployed in parallel at FRIB, enabling the best scheme to be chosen for each specific species of radioactive beam.

There is already significant effort at FRIB being directed towards the (new and unproven) cryogenic gas stopper and cyclotron gas stopper approaches. These two gas-stopper approaches may, however, be limited by space charge issues to incident beam rates of approximately 10^8 pps [4], whereas FRIB is projected to provide fragment beams at unprecedented rates up to 10^{12} particles per second (pps) for many rare isotopes. Obtaining higher incident beam intensities will require a solid stopper approach, which suffers no performance degradation from space charge; this approach may therefore potentially provide the most intense and highest quality beams for certain crucial elements. In particular, low-energy beams of ^{22}Na,

^{23}Mg, ^{25}Al, ^{27}Si, ^{29,30}P, ^{33,34}Cl, ^{35}Ar, and ^{37,38}K with intensities > 10^{10} pps intensities, needed for the measurements of important capture reactions for nuclear astrophysics, may be most readily produced with a solid stopper system. Since high beam intensity and quality is a key to new science and discovery in studies with short-lived nuclei, developing a robust solid stopper scheme is critical to establishing a world leadership position for the FRIB science program.

A solid stopper bears a strong resemblance to the targets used in the Isotope Separator On-Line (ISOL) method [5] of RIB production. In the ISOL approach, a light ion (proton or deuteron) beam strikes a target and, via one or more types of nuclear reactions with nuclei in the target material, produces a short-lived radioactive nucleus of interest within the target. If the target material is heated, the radioactive species can diffuse out of the target and subsequently effuse through a vapor-transfer tube to an ion source, where it can be ionized and subsequently reaccelerated. In a solid stopper system, the fast radioactive ions produced via a fragmentation process will enter the stopper material and through interactions will lose energy, slow down, be neutralized, and stop (be thermalized). The thermalized fragment atoms will diffuse out of the heated stopper material and effuse to an ion source where they are ionized and injected into an accelerator to boost them to the energy needed for use in experiments. In both approaches, it is crucial to reduce the diffusion and effusion times as much as possible so that shorter-lived radioactive species may be ionized.

Although a solid stopper is similar to an ISOL target, it will face a number of novel design challenges, first of which is withstanding the irradiation of high-energy heavy fragment ions. To remove beam-deposited heat from the system, proper design geometry, combinations of materials, and cooling channels can be utilized. Upstream energy degraders may also be used prior to the stopper to slow down the fragment beams. This can reduce the radiation damage of the stopper entrance window and the stopper material and, at the same time, can reduce the stopper dimensions and thus the required diffusion and effusion distances of the released species. Similar considerations apply for the geometry (shorter is better) and material (chemically inert will reduce surface adsorption) of the vapor transfer tube to enable the fastest possible effusion of the fragment atoms into the ion source. Another challenge is to choose a target material (*e.g.*, graphite) that can withstand high temperatures (typically 1500 °C – 2000 °C), which are needed to improve the efficiency of the diffusion and effusion processes, without excessive vaporization/sublimation that would erode the target and degrade the system vacuum. Experimental investigation of the parameter space for these solutions is impractical because the required high-energy, heavy ion beams needed for a systematic design study would be very difficult to obtain. Computational simulations are, however, a viable approach for the initial design of a solid stopper system.

An R&D effort has been initiated at ORNL to utilize our extensive expertise in ISOL target systems to develop a solid stopper system for use at FRIB. We have performed extensive simulations to address the

major challenges, including thermal issues and decay losses from diffusion and effusion delay times, to determine the best choices of stopper material, system geometry, and operating conditions to produce radionuclides of interest. The result of these studies is a proof-of-concept solid stopper system that can provide sufficiently prompt and efficient release of short-lived radionuclides.

Our approach has six steps: (1) Select and evaluate suitable materials for stopping the fast fragments and releasing them to an ion source; (2) Model the projectile/stopper interaction processes; (3) Simulate the beam heating effect and the equilibrium temperature distributions in the stopper materials; (4) Model the diffusion and effusion processes; (5) Integrate the computational models and tools to achieve an end-to-end system design workflow; and (6) Evaluate a set of solid stopper designs to find a proof-of-concept with potential prompt and efficient release of selected radionuclides. This report summarizes our results.

2. COMPUTATIONAL CODES

Extensive computational studies for ISOL target and ion source systems have previously been reported. In those studies, the beam heating, diffusion, and effusion processes are simulated separately with different software codes. For example, the finite elements codes ANSYS [6, -] and COMSOL [7] were used to calculate the temperature distributions in ISOL target assemblies due to beam heating, applied heating, and external cooling [8, 15]. The diffusion delays were calculated by analytically solving Fick's equations for simple planar, cylindrical, and spherical geometries [9, 10] or with a finite-difference code [9, 11], while the effusion process was simulated using a Monte Carlo code such as GEANT4 [12,13], MolFlow+ [14], and *effusion* [9, 11, 15]. The overall delay time was then obtained by convolving the diffusion and effusion delays.

It is noted that for all the prior studies, the thermal analyses are decoupled from diffusion and effusion simulations. That is, the temperature distributions of the target and ion source units are not included in modeling the associated diffusion and effusion processes. Instead, an average temperature of the system was used. Consequently, the resulting diffusion and effusion delays may differ from the actual experimental conditions. In the present work, we have integrated the thermal analysis with effusion simulations for a more realistic determination of release times.

After significant evaluations and comparisons, the following computational codes were selected for our solid stopper simulations.

(1). HSC Chemistry [16] was used to evaluate and select the potential stopper materials. HSC is commercial software for thermodynamic calculations of chemical reactions, equilibrium compositions, and phase stability diagrams. It has been previously used to evaluate ISOL target materials [8, 15].

(2). The stopper material must be able to withstand the bombardment of heavy fragment beams. Specifically, as the fragments slow down and come to rest, they transfer energy to the atoms/molecules within the stopping materials, and the resulting heat can cause vaporization and sublimation in the material. The fragment energy loss depends on its mass and energy, as well as the stopper material and density. Two Monte Carlo-based simulation codes, SRIM [17] and LISE++ [18], were selected for simulating the fragment stopping depth profiles (concentration vs. depth) and beam power deposition distributions (power vs. depth) in the stopper materials for selected fragment beams and energies. These data are needed as inputs to subsequent studies of diffusion-effusion release and thermal analysis of the stopper system.

(3). The finite element software COMSOL Multiphysics [8] with its Heat Transfer Module was used for thermal simulations to calculate the heating effects imparted by the fast heavy-ion beams and the temperature distributions within the stopper materials and composite-stopper/heat-sink systems. Such simulations are a crucial means to assess the beam power limits for selected combinations of fragment beams and stopper materials and the efficacy of potential cooling/heating channel designs for temperature control.

(4). The COMSOL Multiphysics with its Particle Tracing Module was used to simulate the effusion process for the neutral species to be transported from the stopper material to the ion source. The Particle Tracing Module is designed to calculate and trace the trajectories of charged or neutral particles which can interact with boundaries and their motion can be affected by various forces.

(5). Diffusion delay times were obtained by analytically solving Fick's equations for simple geometries (planar, cylindrical, and spherical) of the stopper materials. For the present study, we considered stoppers in the form of thin foils for their short diffusion lengths. Diffusion release from thin-foil solid stoppers is primarily in the direction perpendicular to the foil surface, so that the diffusion process can be treated in one dimension. Well-known analytical solutions to Fisk's laws of diffusion in one-dimensional planar geometries with various boundary conditions were used to calculate the diffusion delay times. We then convolved the time delays of the diffusion and effusion processes to determine the *total* delay time from particle stopping to exit from the vapor-transport tube and enter into the ion source.

The use of the COMSOL Multiphysics software platform was essential for our simulations, since it enabled the integration of the thermal and effusion simulations. Specifically, the particle effusion through the stopper and vapor-transfer tube were simulated with the actual temperature distributions from the thermal simulation of the system. To our knowledge, this work is the first to couple the thermal and effusion simulations. In addition, COMSOL has the capability to simulate the diffusion of diluted species through solid materials. That means that it will be possible to couple the thermal, diffusion, and effusion simulations together with COMSOL in future studies.

3. FRAGMENT ION BEAM SPECIES AND PROPERTIES

The fragment beams that are of great interest for solid stopper applications at FRIB include the alkali and alkaline earth elements and noble gas elements [19]. We have used stable isotopes for our simulation studies because the physical and chemical properties relevant to the release of these elements are the same for stable and radioactive isotopes; the decay loss of the radioactive isotopes can be accounted for separately. The estimated beam energy and beam rates [20] for the stable isotopes are given in Table 3-1. The fragment beams are assumed to have a Gaussian profile with a FWHM of 1 cm and 5% maximum energy uncertainty [19], and these beam properties were used in the simulations.

Table 3-1. Fragment beams of interest for a solid stopper system.

Element	Z	A	Frag. E (MeV/u)	Fast Beam Rate (pps)
Li	3	7	251.3	1.27E+11
Be	4	9	248.4	2.74E+11
Ne	10	20	237.7	2.35E+14
Na	11	23	241.5	4.96E+11
Mg	12	24	238.8	5.09E+11
Ar	18	40	216.5	1.42E+14
K	19	39	227.5	7.87E+11
Ca	20	40	226.1	1.41E+14
Kr	36	84	186.1	2.02E+11
Rb	37	85	187.3	2.74E+10
Sr	38	88	187.2	3.56E+10
Xe	54	132	175.6	3.42E+10
Cs	55	133	166.7	9.83E+08
Ba	56	138	166.7	6.73E+08
Rn	86	222	158.8	5.70E+06
Fr	87	223	158.5	2.68E+07
Ra	88	226	158.5	4.90E+07

4. SIMULATION STUDIES AND RESULTS

In the following subsections, we will present details of our simulations of solid stopper systems.

4.1 SELECTING AND EVALUATING SUITABLE STOPPER MATERIALS

The stopping and release of rare isotopes depends on the physical and chemical properties of the specific element of interest as well as the properties of the stopper material(s) and their interactions. The materials must be refractory so that they can be raised to the high temperatures required for fast diffusive release of rare isotopes without excessive vaporization or sublimation. It is also critical that they are chemically inert to (*i.e.*, not form compounds with) the species of interest that would bind them in the stopper. The radioisotope of interest must be able to rapidly diffuse to the surface through the material, either in elemental or molecular form. Finally, upon reaching the surface, the radioisotope must be readily desorbed for effusive transport to the ion source. Based on these primary selection criteria, candidate stopper materials include graphite, refractory metals, oxides, and carbides. For this work, we considered a number of refractory materials; their densities and melting points are listed in Table 4-1.

Table 4-1. Candidate materials for stopping disks and vapor-transfer tubes.

Candidate material	Density (g/cm^3)	Melting temp (^{o}C)
Graphite	2.25	3652
Tantalum	16.6	2850
Molybdenum	10.2	2610
Niobium	8.57	2410
Zirconium	6.49	1852
Vanadium	5.96	1890
Tungsten	19.35	3410
Rhenium	20.53	3170

The properties of the candidate materials can be evaluated using the thermochemical code HSC Chemistry. Figure 4-1a shows an example of the calculated equilibrium components of tantalum and graphite as a function of temperature, assuming the presence of both tantalum and graphite as the stopper and/or construction materials, which is often the case in ISOL target and vapor-transfer systems. The result indicates that Ta and C may react to form carbides, and more importantly, both solid Ta and C will convert to the gas phase at temperatures of 2400 - 2700^{o}C. Hence, the upper operating temperature of the stopper may be limited to about 2400^{o}C to prevent excessive sublimation of the materials. The calculations have

assumed a pressure of $2 \cdot 10^{-4}$ Torr, which is close to the limiting pressure of the electron beam plasma ion source used at HRIBF [15]. For lower pressures, the limiting operation temperature may shift accordingly to lower values. Fig. 4.1b presents the Ta-C phase diagram [21] calculated with a completely independent code together with experimental datapoints, which suggests stable TaC phase between temperatures of 1000 K to 3500 K. Ta_2C has also been reported [22] to be the intermediate product of the TaC conversion. The HSC calculation agrees with the literature results.

Figure 4-2a presents the calculated equilibrium compositions of the Ta, C, and Si system at a pressure of $2 \cdot 10^{-4}$ Torr. Here Si ions are the stopped fragment ions, and therefore the amount of Si is assumed to be 10^4 times smaller than the amounts of Ta and C. The HSC calculation suggests that Si may react with C, usually under high temperatures, to form SiC. Once formed, SiC is stable at all temperatures until significant sublimation of graphite takes place. Thus, C may not be a suitable stopper material for stopping and releasing Si isotopes. In a similar fashion, we compare our HSC calculations for the Si + C system to literature data [23] and found very good agreement (Fig. 4-2b). For a beam of K ions (Figure 4-3), our calculations indicate that K will not form refractory products with Ta and C and can be easily released as gaseous species even at temperatures well below 500°C. These examples show that suitable stopper materials must be evaluated for each individual beam.

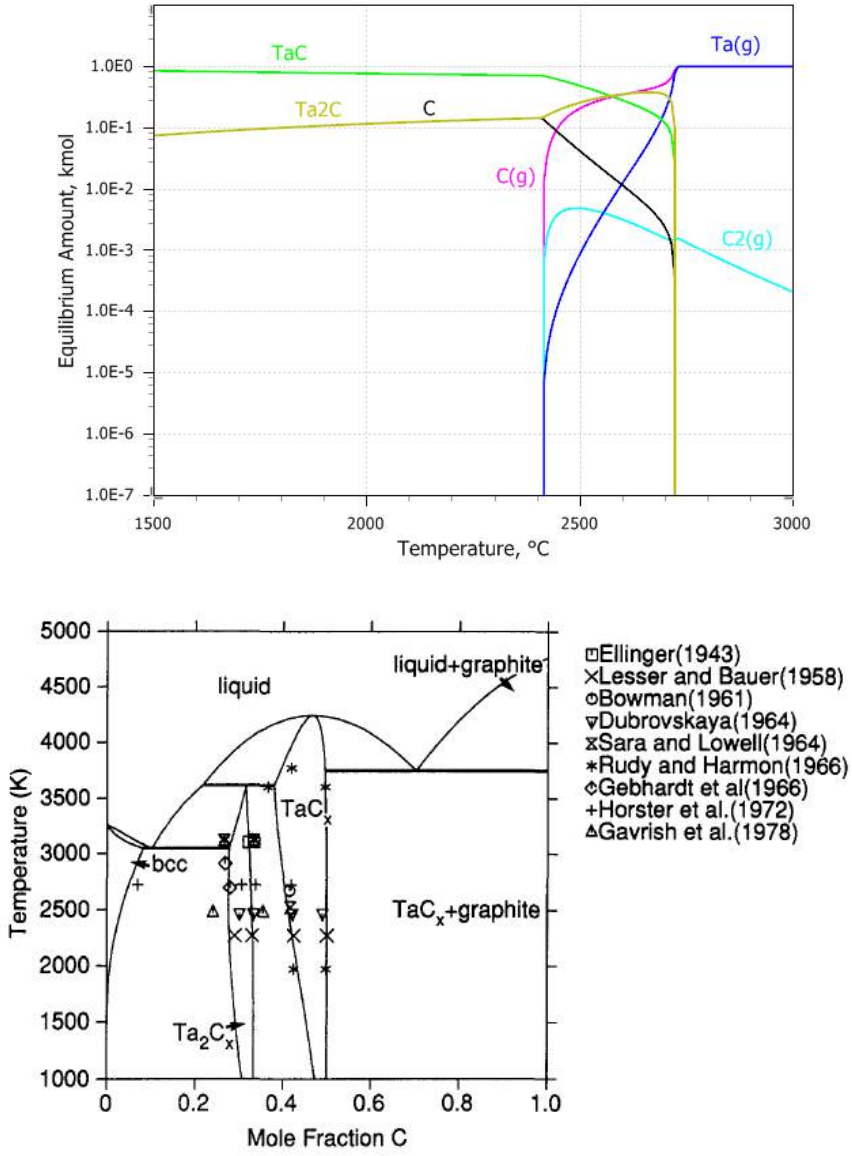

Figure 4-1. (a) HSC calculation results of the equilibrium compositions of Ta + C system versus temperature at a total pressure of $2 \cdot 10^{-4}$ Torr. Ta and C are assumed to have equal initial amounts of 1 kmol. In this and in Figure 4-2 and 4-3, the suffix "(g)" stands for gaseous species and the species without any suffix are solid species. (b) The calculated Ta-C phase diagram with experimental data points on phase boundaries (from Ref. 21).

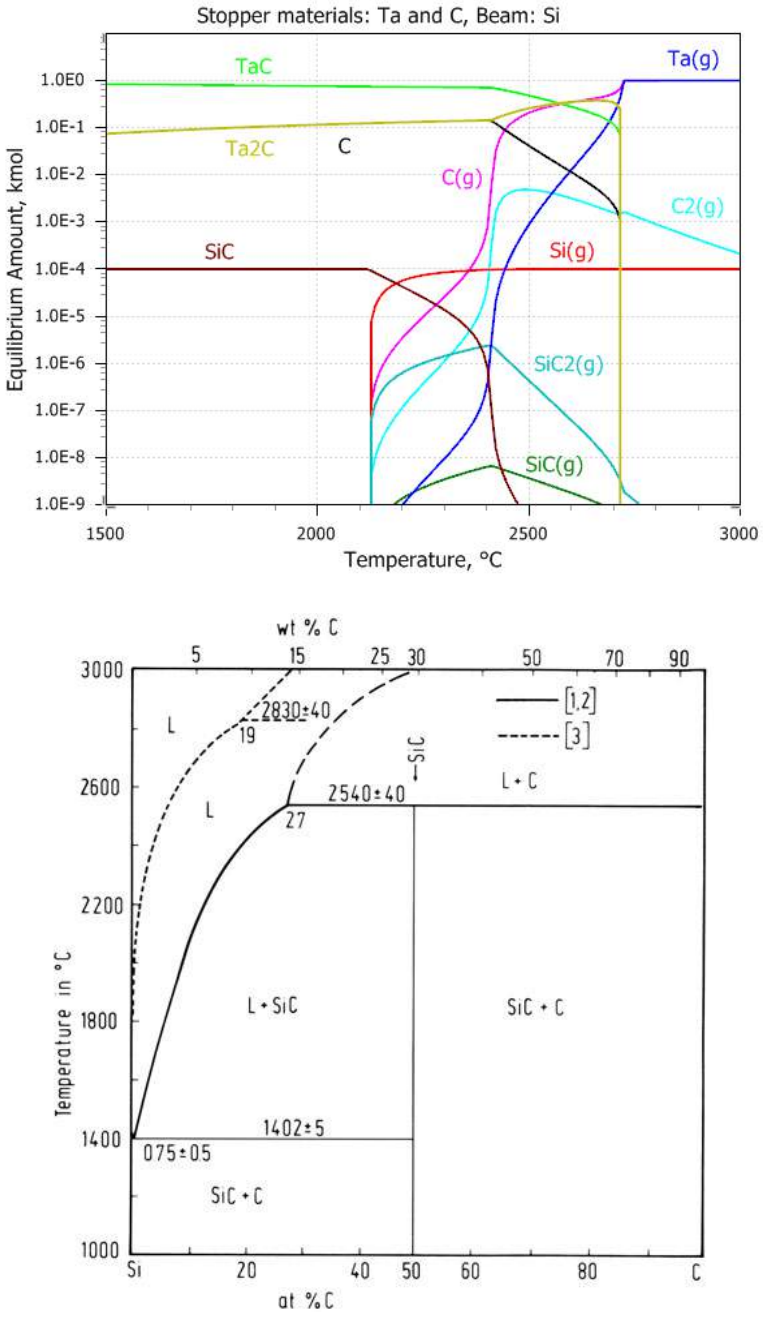

Figure 4-2. (a) Equilibrium compositions of Ta, C, and Si at a pressure of $2 \cdot 10^{-4}$ Torr. Ta and C are assumed to have equal initial amounts of 1 kmol and the amount of Si is 10^4 times less than those of Ta and C. SiC will convert to gaseous Si at temperatures above 2100 °C. (b) The phase diagram of Si-C system from Ref. 23.

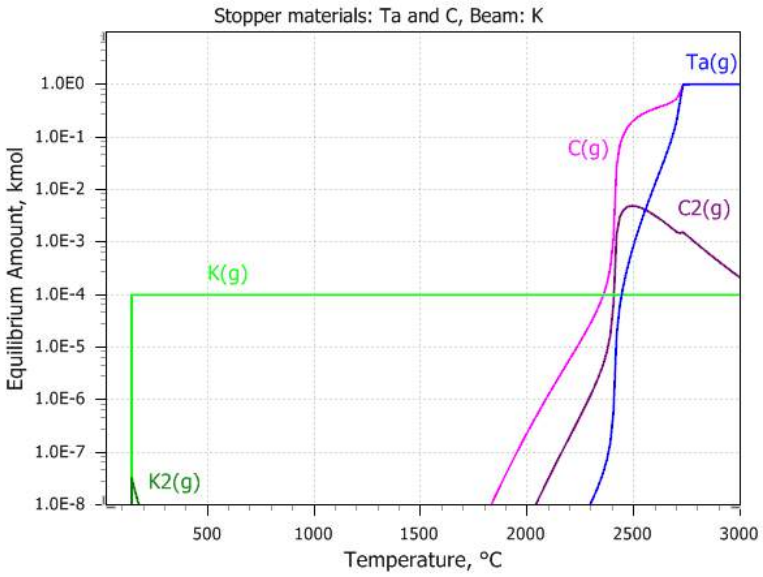

Figure 4-3. Equilibrium gas phase composition of Ta, C, and K at a system pressure of 2•10^{-}4 Torr. Ta and C are assumed to have equal initial amounts and the amount of K is 10^4 times less than those of Ta and C.

4.2 MODELING PROJECTILE/STOPPER INTERACTIONS

Two codes, SRIM and LISE++, were used to simulate the stopping power and energy deposition of the beams in stopper materials. The results of these calculations served as inputs to the thermal simulations for beam induced heating and temperature distributions in the stopper.

Figure 4-4 shows the calculated Li stopping powers in tantalum in the longitudinal direction. As noted, near the stopping position, there are significant deviations in the stopping power profiles between the SRIM and LISE++ calculations, with the peak stopping differing by a factor of ~2. The deviations are likely due to the fact that LISE++ uses a more realistic Monte Carlo method that incorporates initial ion beam emittances as well as energy and angular straggling to calculate the stopping power distributions, while the SRIM data are obtained from the stopping and range tables and do not incorporate those beam properties. For this reason, we relied on LISE++ for the majority of our beam power deposition calculations.

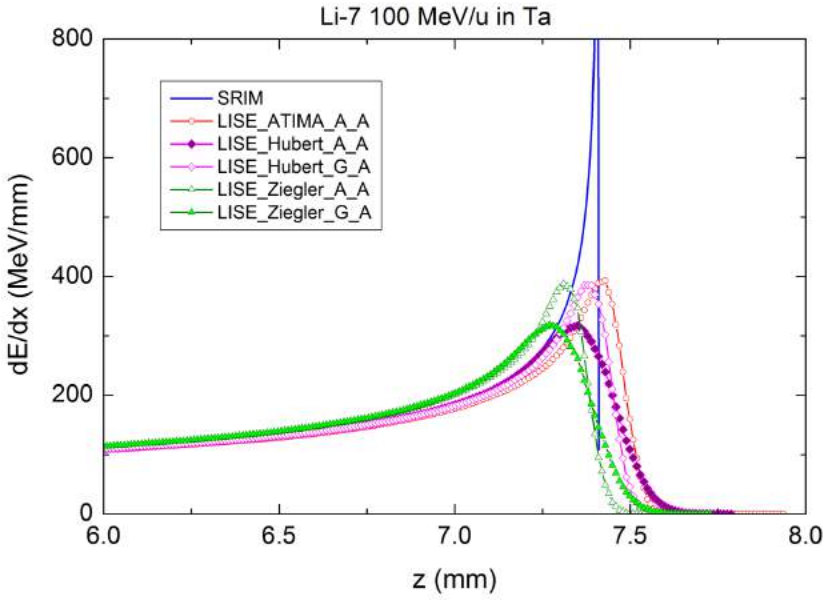

Figure 4-4. Comparison of the Li stopping powers in Ta calculated with SRIM and LISE++. Different LISE++ curves are obtained with the different physics models for energy loss, energy straggling, and angular straggling that are options within the code.

4.3 SIMULATING HEAT TRANSFER AND EQUILIBRIUM TEMPERATURE DISTRIBUTIONS IN STOPPERS

As the ions are slowed down and come to rest in the stopper, the beam energy is absorbed in the material and transformed into heat. When the heat deposited by the incident beam is too high, the stopper should have effective cooling channels to prevent vaporization/sublimation of the stopper materials. When the beam heating is too low to raise the temperature necessary for optimal release of the radionuclides of interest, the stopper needs to be heated by external means to reach the desired temperature. Thermal simulations are therefore essential to understand the possibility of controlling the stopper temperature for optimal radionuclide release and minimal stopper damage. We have used COMSOL's Heat Transfer Module to simulate the beam heating effects on the stopper. The heat transfer in the solid stopper is simulated in COMSOL by solving the heat equations given by

$$\rho C_p \frac{\partial T}{\partial t} + \nabla \cdot q = Q \tag{1}$$

$$q = -k\nabla T \tag{2}$$

where T is the absolute temperature (K), $\boldsymbol{q}$ is the heat flux (W/m^2), Q is the beam deposited heat source (W/m^3), and ρ, C_p, and k are the density (kg/m^3), specific heat capacity (J/(kg•K)), and thermal conductivity (W/(m•K)) of the materials, respectively. The stopper material is assumed to be homogenous. The fragment ion beam flux is modeled with a Gaussian function of the form

$$I(x,y) = \frac{I_t}{2\pi\sigma^2} \exp\left(-\frac{x^2+y^2}{2\sigma^2}\right) \quad (3)$$

where I_t is the ion beam intensity and x and y are spatial coordinates transverse to the beam propagation direction z. The full width at half maximum (FWHM) of the Gaussian profile is given by

$$FWHM = 2\sqrt{2\,ln2}\,\sigma \quad (4)$$

The heat deposited in the stopper material by the beam can then be expressed as

$$Q(x,y,z) = \frac{I_t}{2\pi\sigma^2} \exp\left(-\frac{x^2+y^2}{2\sigma^2}\right) \frac{dE}{dz} \quad (5)$$

where dE/dz is the stopping power of the stopper material as a function of z calculated with LISE++, as discussed above.

We developed numerous steady-state geometrical models to calculate the 3D equilibrium temperature distributions in various stopper systems. Figure 4-5 shows an example of a stopper consisting of three stopper disks held in a cylindrical container.

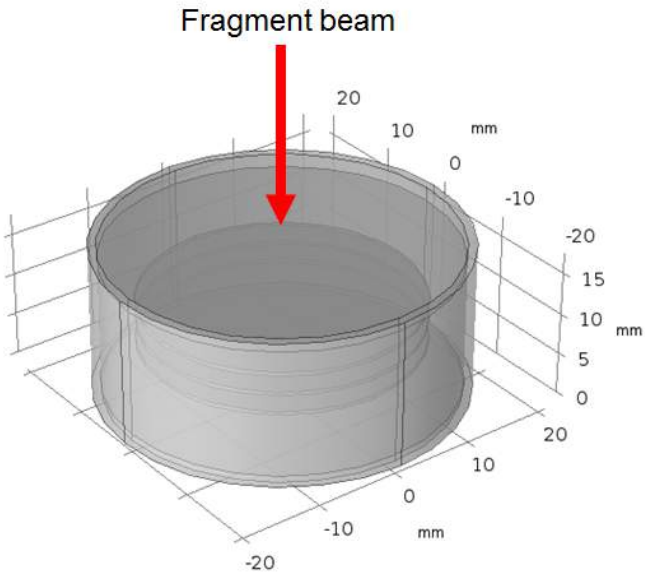

Figure 4-5. Geometrical model for thermal simulations of a stopper with three stopping disks in a cylindrical holder, heated by an incident fragment ion beam.

We simulated the bombardment of this stopper by a 187 MeV/u ^{88}Sr fragment beam. According to our HSC calculations, Ta and C would be suitable stopper materials for Sr. As shown in Figure 4-6, Sr may react with C to form SrC_2, but it will convert to atomic Sr vapor –above 1000 ^{o}C. The stopping ranges of the Sr beam in tantalum and graphite, as calculated with LISE++, are shown in Figure 4-7.

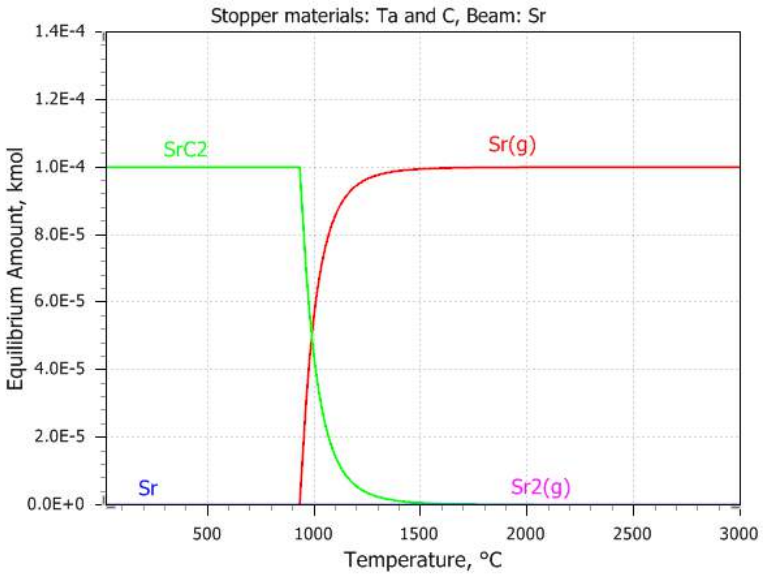

Figure 4-6. Equilibrium components of Sr species of the Ta-C-Sr system at a pressure of $7.5 \cdot 10^{-5}$ Torr. Ta and C are assumed to have equal initial amounts of 1 kmol and the amount of Sr is 10^4 times less than those of Ta and C. Sr is converted to gas phase at temperatures above 1000 °C.

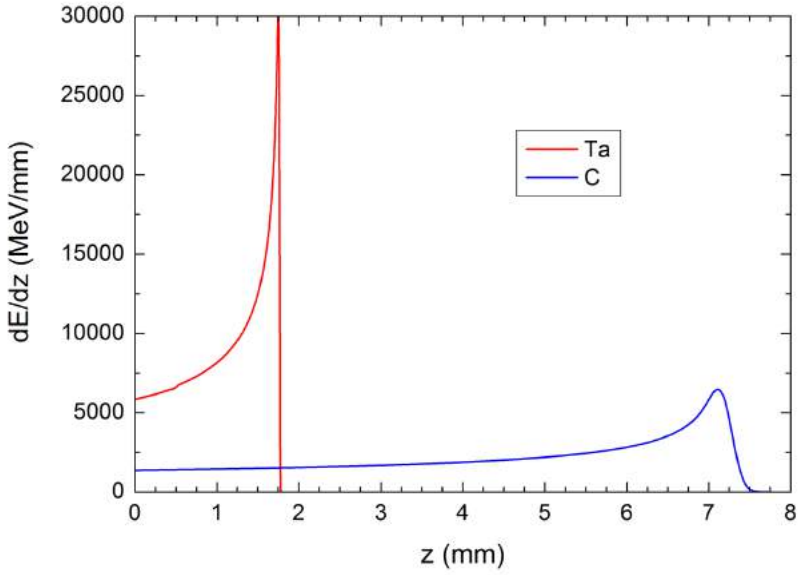

Figure 4-7. Stopping power of 187 MeV/u ^{88}Sr ions as a function of depth in Ta and graphite.

Our first model contained a 0.75-mm thick Ta window and three 0.4-mm thick Ta stopper disks. Assuming a Gaussian shape with $\sigma = 4$ mm and a FWHM = 9.42 mm for the Sr beam [19], we selected the radius of the stopper disks to be $r = 4\sigma = 16$ mm. The stopper holder was a Ta cylinder of 40 mm ID, 17.6 mm in

length, and with a 1 mm wall thickness. Beam heating by Sr beams of intensities 0.1, 1.0, and 10 nA were simulated, as the ^{88}Sr beam rate at FRIB was estimated to be $3.56 \cdot 10^{10}$ pps (Table 3-1). The thermal simulation included the following physical effects:

(1) heat transfer in all solid materials by conduction;
(2) heat transfer between surfaces by surface-to-surface radiation; and
(3) heat transfer from the external surface of the cylindrical holder by radiation to ambient (*i.e.*, room) temperature (293.15K).

The calculated equilibrium temperature distribution in the stopper heated by 10 nA ($6.25 \cdot 10^{10}$ pps) Sr beam is shown in Figure 4-8. Figure 4-9 presents the radial temperature distributions in the three Ta disks for 0.1 nA, 1 nA, and 10 nA Sr beams, respectively. These results suggest that with a 0.1 nA beam, the stopper temperature is less than 500 °C, below the minimum temperature for Sr release (Figure 4-6) and external heating will be necessary to heat the stopper disks to release the Sr. For 1 nA and 10 nA beams, external heating is also desired to raise the stopper temperature to the upper limit (~2400 °C) for faster diffusion and effusion release.

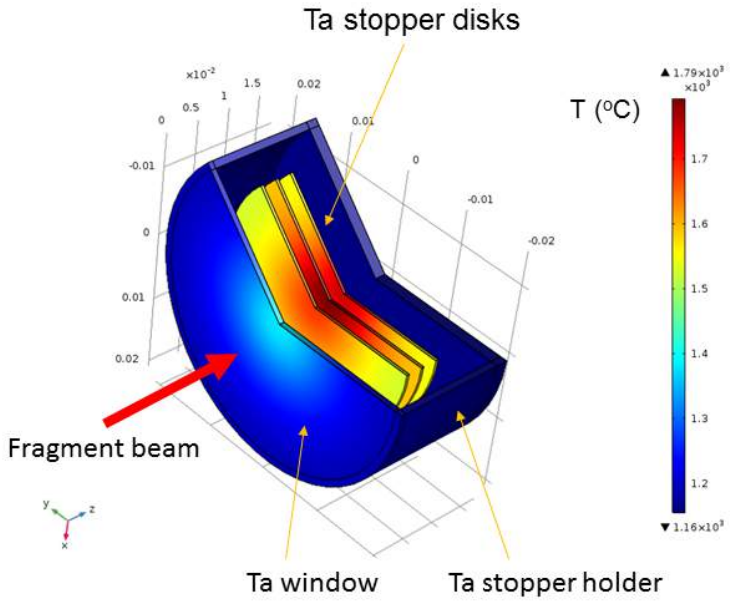

Figure 4-8. Equilibrium temperature distribution in the stopper with three Ta disks (0.4 mm thick) and a 0.75-mm thick Ta window for stopping 10 nA ^{88}Sr beam particles of energy 187 MeV/u.

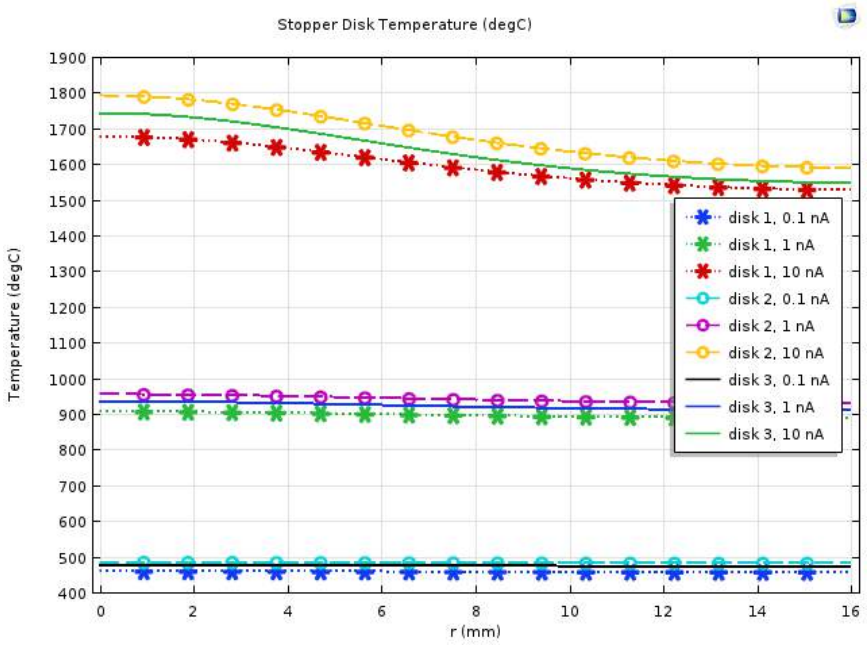

Figure 4-9. Equilibrium temperature distribution in the stopper disks resulting from a 0.1, 1, and 10 nA incident ^{88}Sr beam of energy 187 MeV/u passing through a 0.75-mm thick Ta entrance window and then successively into 0.4-mm thick Ta stopping disks 1, 2, and 3

The second model (Figure 4-10) used graphite as the stopping disk material. Since graphite has much lower stopping power than tantalum (Figure 4-7), an Al degrader (3 mm thick) is used in front of the stopper. In this case, the stopper is heated to lower temperatures by the same 10 nA Sr beam, but the temperature in the Al degrader well exceeds the material's melting temperature, as shown in Figure 4-11. Therefore, external heating will be needed to heat the graphite stopper disks while cooling for the Al degrader is necessary. We realize that the degrader we used in Fig. 4-10 is not a realistic representation of those that will be used at FRIB. However, our simple degrader model effectively demonstrates that the total thickness of the stopper material can be significantly reduced when beam momentum is lost upstream in the degrader.

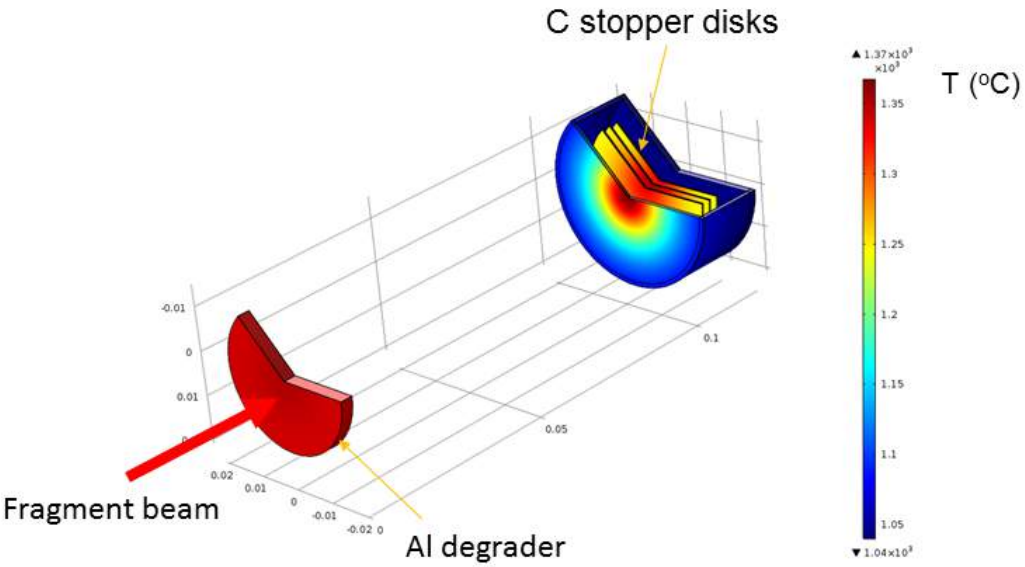

Figure 4-10. Equilibrium temperature distribution in the stopper disks resulting from a 10 nA incident ^{88}Sr beam of energy 187 MeV/u passing through an Al degrader (3 mm thick) and then successively into the stopper with a 0.75 mm Ta window and three 0.4-mm thick C stopping disks.

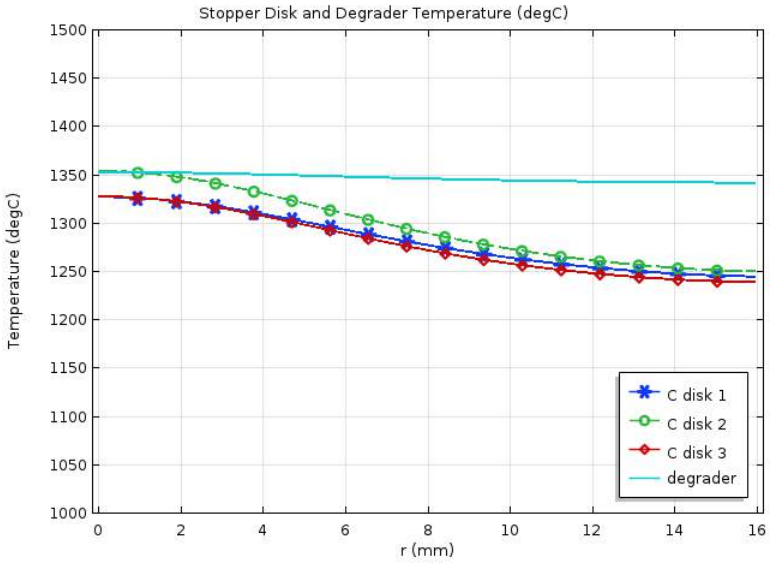

Figure 4-11. Axial temperature distributions of the graphite disks and the Al degrader heated by 10 nA ^{88}Sr beam. C disk 1 is the first disk after the Ta entrance window. The temperature in the Al degrader is around 1350 °C, much higher than the material's melting point of 660.32 °C

4.4 SIMULATING DIFFUSION

The mathematical theory of diffusion in an isotropic medium is based on Fick's first and second laws

$$J = -D\,\nabla C \tag{6}$$

$$\frac{\partial C}{\partial t} = D\,\nabla^2 C \tag{7}$$

where J is the flux of the diffusing substance (particles/cm^2/s), C is the concentration of diffusing substance (particles/cm^3), and D is the diffusion coefficient (cm^2/s). Equation (7) assumes that D is a constant, which is usually a good assumption for diffusion in solids.

In thin-foil solid stoppers, release of the stopped fragments by diffusion is primarily in the direction perpendicular to the foil surface. Thus, the diffusion process can be approximated by the following one-dimensional diffusion equation:

$$\frac{\partial C}{\partial t} = \mathrm{D}\frac{\partial^2 C}{\partial x^2} \qquad (0 \le x \le h) \tag{8}$$

where h is the foil thickness. Assuming the following initial and boundary conditions:

$$C(x,t) = C_0 \qquad (t = 0,\ 0 < x < h) \tag{9}$$

$$C(x,t) = 0 \qquad (t \ge 0,\ x = 0\ and\ x = h\,) \tag{10}$$

These conditions assume that the stopped fragments are uniformly distributed inside the thin foil at the beginning, and upon diffusing to the surfaces they are instantly desorbed. Hence, the solution to Eq. (8) is

$$C(x,t) = \frac{4C_0}{\pi}\sum_{n=0}^{\infty}\frac{1}{2n+1}\exp\left[-\frac{D(2n+1)^2\pi^2 t}{h^2}\right]\sin\left[\frac{(2n+1)\pi x}{h}\right] \tag{11}$$

The fraction of the fragments retained in the stopper foil at time t, $F(t)$, is given by integrating $C(x,t)$ with respect to x between $x = 0$ and $x =$ h and divided by the initial amount C_0h:

$$F(x,t) = \frac{1}{C_0 h}\int_0^h C(x,t)\,dx = \frac{8}{\pi^2}\sum_{n=0}^{\infty}\frac{1}{(2n+1)^2}\exp\left[-\frac{D(2n+1)^2\pi^2 t}{h^2}\right] \tag{12}$$

The fractional diffusion release rate, $R(t)$, expressed in terms of the fraction of the fragments diffusing out of the thin foil surfaces per unit time is given by

$$R(t) = -\frac{\partial F}{\partial t} = \frac{8D}{h^2}\sum_{n=0}^{\infty} exp\left[-\frac{D(2n+1)^2\pi^2 t}{h^2}\right] \tag{13}$$

The characteristic diffusion time τ_d is defined as

$$\tau_d = \frac{h^2}{\pi^2 D} \tag{14}$$

which corresponds to the time at which ~70% of the particles have diffused out. Then Eq. (13) for $R(t)$, the fraction of the fragments diffusing out of the thin foil surfaces per unit time, can be rewritten as

$$R(t) = \frac{8\pi^2}{\tau_d} \sum_{n=0}^{\infty} exp\left[-\frac{(2n+1)^2 t}{\tau_d}\right] \tag{15}$$

This expression for diffusion is convoluted with the numerical simulation of effusion to determine the total release time of atoms from the system as described below in Section 6.6.

4.5 SIMULATING EFFUSION

When stopped fragment species diffuse to the surface of the stopper materials, they desorb from the surface and undergo a series of collisions with walls and stoppers in the stopper holder until they escape to the ion source through the vapor-transfer tube. To maximize the resultant radioactive beam current, the time spent in this random-walk effusion process should be as short as possible to minimize losses from radioactive decay. We focused our simulation efforts on effusion simulations since they provide critical information for determining the geometry, dimension, and configuration of the stopper and vapor transport system.

Our effusion simulations were conducted with the Particle Tracing Module in the COMSOL Multiphysics software platform. For free molecular flows, the particle trajectories are computed using Newton's law of motion:

$$\frac{d}{dt}\left(m\frac{d\boldsymbol{q}}{dt}\right) = \boldsymbol{F} \tag{16}$$

where m is the particle mass, $\boldsymbol{q}$ is the particle position vector, and $\boldsymbol{F}$ is the force exerted on the particle. The particle velocity $\boldsymbol{v}$ is given by:

$$\boldsymbol{v} = \frac{d\boldsymbol{q}}{dt} \tag{17}$$

The effusion process is calculated using the Monte Carlo method wherein the trajectories of large numbers of particles with randomized initial conditions are computed as they move through the stopper holder and the vapor-transfer tube. Each particle is traced from injection until it reaches the outlet boundary. The number of particles that reach the outlet determines the transmission probability. The transmission probability is obtained as a function of time, as shown in Figure 4-12. The characteristic effusion delay time, t_c, is extracted by fitting the time-dependent transmission curve to the following equation:

$$f(t) = 1 - \exp(-\frac{t}{t_c}) \tag{18}$$

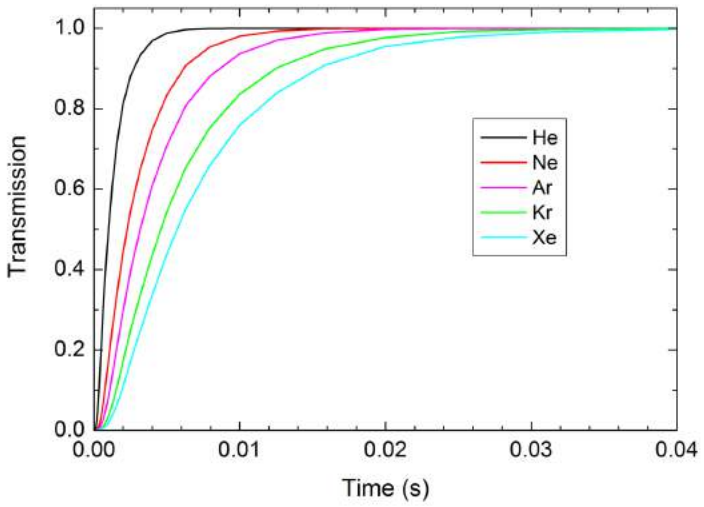

Figure 4-12. Typical transmission curves from COMSOL effusion simulations.

In our COMSOL effusion simulations, we assumed:

(1). Particle movement is under free-molecular flow condition, that is, no collisions between particles.

(2). Particles have an initial Maxwell-Boltzmann velocity distribution.

(3). When particles encounter a surface or wall, they are re-emitted according to Knudsen's cosine law [24].

(4). At each surface collision, particles are thermalized and re-emitted with a Maxwell-Boltzmann velocity distribution of the surface temperature where they hit.

(5). Surface adsorption is represented by a mean sticking time τ_a given by

$$\tau_a = \tau_0 \exp\left(\frac{E_a}{k_B T}\right) \tag{19}$$

where E_a is the activation energy for desorption, k_B is the Boltzmann's constant, and $\tau_0 \sim 10^{-13}$ s [6].

4.5.1 Validation of Effusion Simulations

We validated the results of our COMOSL effusion calculations via analytical calculations for standard problems as well as comparisons with experimental data and previous simulation results. These validations are presented below.

4.5.1.1 Clausing factor determination

Our first validation was to use our simulations to determine the well-known Clausing factor [25] of cylindrical tubes. The Clausing factor (α) is the probability that a particle entering the tube at one end will

escape at the other end after making collisions with the wall of the tube. We determined the Clausing factors in simulations of two geometries where an analytical solution is available:

(a). Cylindrical tubes (Figure 4-13 left) of radius *R* and length *L*;

(b) Cylindrical annulus (Figure 4-13 right) of length *L*, inner radius *R1*, and outer radius *R2*.

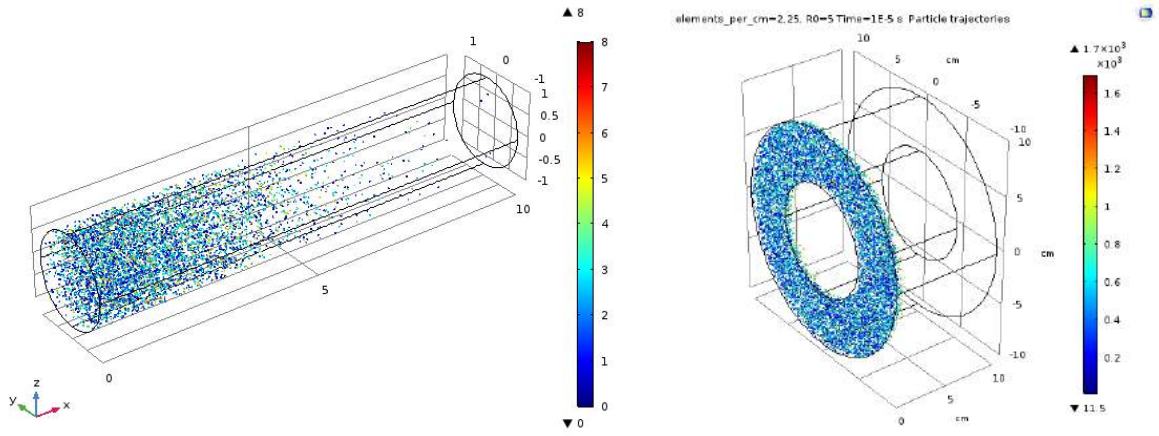

Figure 4-13. COMSOL models for Clausing factor determination: (left) cylindrical tube and (right) cylindrical annulus.

Each simulation utilizes a Monte Carlo approach wherein 10,000 particles are injected into the tubes from the inlet surface (on the left in Figure 4-13) with randomly sampled positions and cosine angular distributions. The walls have a sticking probability of 0. Particles are assumed to be lost when they pass through the outlet surface (the end face on the right) or bounce back and pass the inlet surface. The Clausing factor or transmission probability is then determined as the ratio of the number of particles reaching the outlet surface to the total number of particles injected. For each set of tube radius and length values, we ran at least three such simulations and chose the Clausing factor as the mean value of the calculation results and the simulation uncertainty as the standard deviation of the mean.

Table 4-2 gives the COMSOL simulation results for the Clausing factors (α) and uncertainties of cylindrical tubes, compared with previously published analytical and Monte Carlo values. Similarly, the results for a cylindrical annulus are listed in Table 4-3. As shown, the COMOSL results agree very well with the literature values for both geometries.

Table 4-2. The Clausing factors of cylindrical tubes from COMSOL effusion simulations compared to literature values.

L/R	α	Uncertainty	Analytical [26]	Ref. [27]	Ref. [25]	Ref. [14]
0.1	0.9523	0.0014	0.9525	0.95240	0.9524	
0.2	0.9095	0.0020	0.9097	0.90922	0.9092	
0.5	0.8004	0.0027	0.8027	0.80127	0.8013	
1	0.6747	0.0031	0.6737	0.67198	0.6718	0.67946
2	0.5143	0.0047	0.5143	0.51423	0.51364	0.51418
3	0.4215	0.0042	0.4188	0.42006	0.42045	0.42002
4	0.3570	0.0049	0.3548	0.35657	0.3589	0.35651
5	0.3106	0.0046	0.3087	0.31053	0.31458	0.31046
6	0.2753	0.0052	0.2737	0.27244	0.28068	0.27541
7	0.2473	0.0036	0.2462	0.24774	0.25368	0.24772
8	0.2268	0.0025	0.2239	0.22526	0.23155	0.22525
9	0.2090	0.0041	0.2055	0.20664	0.21304	0.20660
10	0.1910	0.0031	0.1899	0.19094	0.19729	0.19090
20	0.1096	0.0034	0.1093	0.10932	0.11352	0.10929
50	0.0480	0.0022	0.0487	0.04848	0.04988	0.04846
100	0.0250	0.0016	0.0254	0.02528	0.02578	0.02528

Table 4-3. The Clausing factors of cylindrical annuli from COMSOL effusion simulations compared to literature values.

R1/R2	L/R	α	Uncertainty	Ref. [28]	Ref. [11]
0.25	1	0.6151	0.0045		0.614(2)
0.5	1	0.5293	00020	0.5295	0.530(2)
0.75	1	0.3906	0.0056	0.3872	0.385(2)
0.25	2	0.4579	0.0032		0455(2)
0.5	2	0.3784	0.0024	0.3761	0.375(2)
0.75	2	0.2582	0.0059	0.2559	0.256(1)
0.25	5	0.2694	0.0038		0.267(1)
0.5	5	0.2117	0.0025	0.2081	0.209(1)
0.75	5	0.1338	0.0019	0.1310	0.130(1)
0.25	10	0.1616	0.0032		0.163(1)
0.5	10	0.1209	0.0019	0.1216	0.121(1)
0.75	10	0.0747	0.0004		0.0724(8)

4.5.1.2 Effusion time in HRIBF target/ion source system

For further validation, we compared COMSOL simulations for ISOL target/ion source systems with previous experimental measurements and simulations. Figure 4-14 shows the ORNL HRIBF serial-coupled target and ion source assembly and the vapor-transport system. The effusion time through this system was previously experimentally measured with a fast-valve system [15, 29] and was previously simulated using GEANT4 [12, 30].

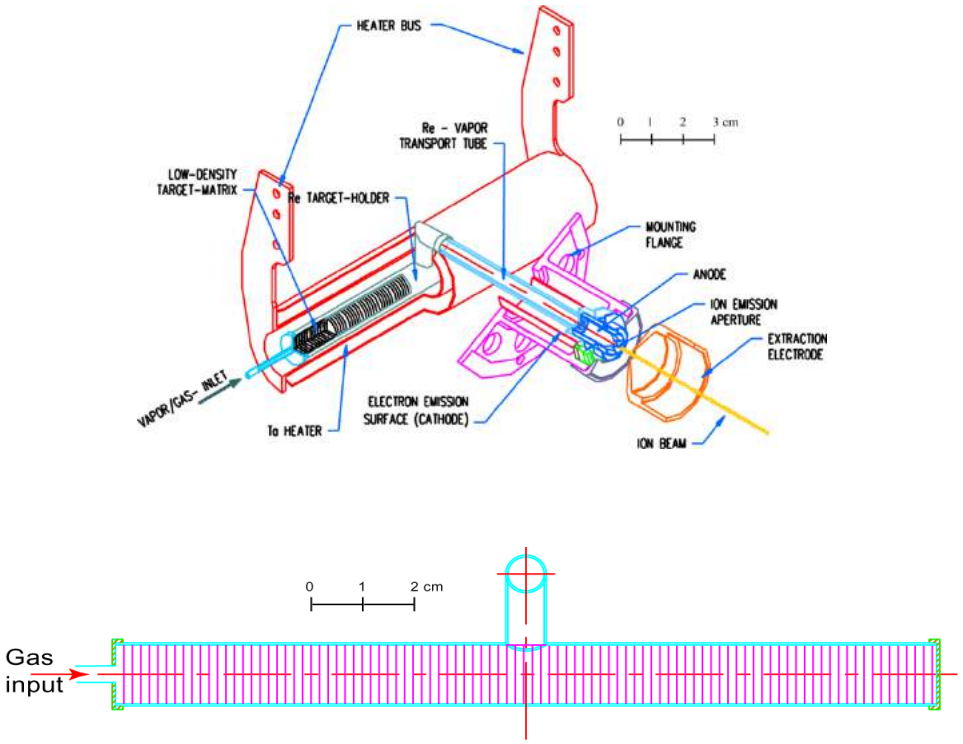

Figure 4-14. HRIBF serial-coupled target and ion source assembly.

Figure 4-15 shows the COMSOL model for the HRIBF system. It has a target reservoir (15.38 mm ID and 193 mm long) and a vapor-transfer tube that is vertically attached to the mid-point of the reservoir and then bent horizontally at 25 mm above the reservoir. The transfer tube has an ID of 8.5 mm and a total length of 135 mm including the elbow. For the purpose of validation, our simulations are conducted without the ion source and without any target materials in the target reservoir.

Particles in our simulation are released into the target reservoir at time $t = 0$ from one end face with a randomly sampled position, a speed taken from a Maxwell-Boltzmann distribution, and a cosine angular distribution of the velocity vector. In this simulation, particles are re-emitted from all surfaces, including the release surface, except the end face of the transfer tube. For each calculation, 10,000 particles are traced until they all have reached the end face (exit) of the transfer tube. Since we only compare with the experimental measurements made with noble gases, no surface sticking is considered in our simulations. The effusion time t_c is obtained by fitting the transmission curve using Eq. (14).

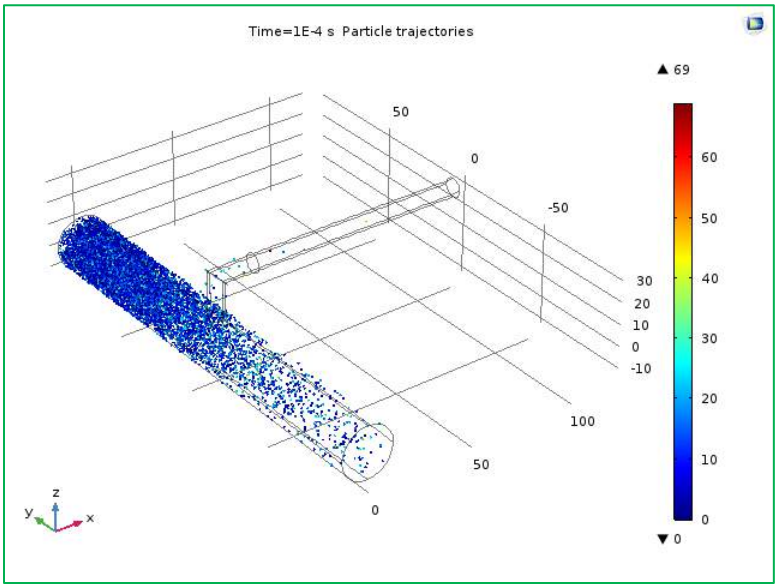

Figure 4-15.COMSOL effusion model representing the ORNL HRIBF serial-coupled target-reservoir and vapor-transfer system.

Figure 4-16 shows the effusion time t_c from COMSOL simulations compared with the experimentally measured [15] characteristic effusion time τ_c for noble gases as well as the analytical formula [6]:

$$\tau_c = \frac{3}{4}\frac{L_{avg}}{v_{avg}} \tag{20}$$

where L_{avg} is the average distance traveled by the particles and $v_{avg} = (8kT/\pi/M)^{1/2}$ is the mean velocity of the particle of mass M at temperature T. The value of L_{avg} was determined by fitting the slope of the experimental τ_c data versus $T^{-1/2}$ for the noble gases [15]. Our COMSOL results agree well with the experimental data and the analytical formula for light gases and are within the uncertainty of the analytical value for Xe**.**

We also compared the results of our COMSOL simulations with that of previous simulations using the Monte Carlo code GEANT4, as given in Table 4-4, and we find that the two approaches are in close agreement. It is interesting to note that for the case of a target reservoir ID = 24 mm, the effusion times from COMSOL and GEANT4 simulations are close, but both are noticeably larger than the experimental data. The average number of surface collisions $<N_{collisons}>$ that the particles will encounter in the target reservoir and vapor-transfer system obtained with COMOSL is smaller than that obtained with GEANT4, but the uncertainty is sufficiently large to include the GEANT4 value. No uncertainty is given for the number of collisions in the GEANT4 simulations.

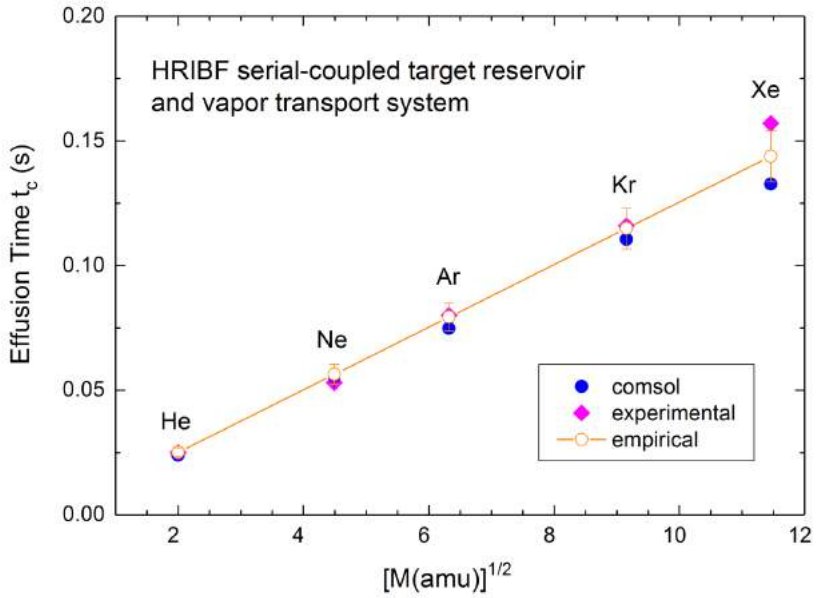

Figure 4-16. Comparison of the calculated effusion time, t_c, vs. $M^{1/2}$ for noble gases of mass M from COMSOL with the experimental data and analytical calculations at a temperature of 1306 K. The analytical points are calculated from Eq. 20 with the experimental *uncertainties in the* τ_c *and* L_{avg} *values.*

Table 4-4. Comparison of COMSOL results with GEANT4 simulations and experimental data for He particles at temperature T = 1473 K.

Target reservoir ID (mm)	COMSOL		GEANT4 [30]		Experiment t_c (ms) [30]
	t_c (ms)	$\langle N_{collisions} \rangle$	t_c (ms)	$\langle N_{collisions} \rangle$	
15	21.7(2)	2884 ± 2700	19.1	4466	23.0
24	49.1(5)	4340 ± 4147	46.8	6540	38.1

4.5.1.3 Effusion time dependence on particle mass and temperature

According to the kinetic theory of gases, the effusion time of a gas is proportional to the square root of the mass of its particles and inversely proportional to the square root of temperature [29]. We confirmed that these general properties are present in our COMSOL simulations for noble gases. For example, we show that the effusion time t_c of the HRIBF serial-coupled target and transport system is a linear function of $M^{1/2}$ in Figure 4-16, and that the calculated effusion time through a cylindrical tube with COMSOL has a linear dependence with $T^{-1/2}$ in Figure 4-17. These properties allow us to carry out effusion simulations for one specific particle mass and temperature, and then use this to obtain the corresponding effusion times for different particles and different temperatures according to the $M^{1/2}$ and $T^{-1/2}$ scaling laws, for the cases where surface sticking can be ignored. For this reason, the effusion simulations presented in the next sections for a wide range of solid stopper assembly configurations are mostly conducted for Sr atoms and T = 1000 K.

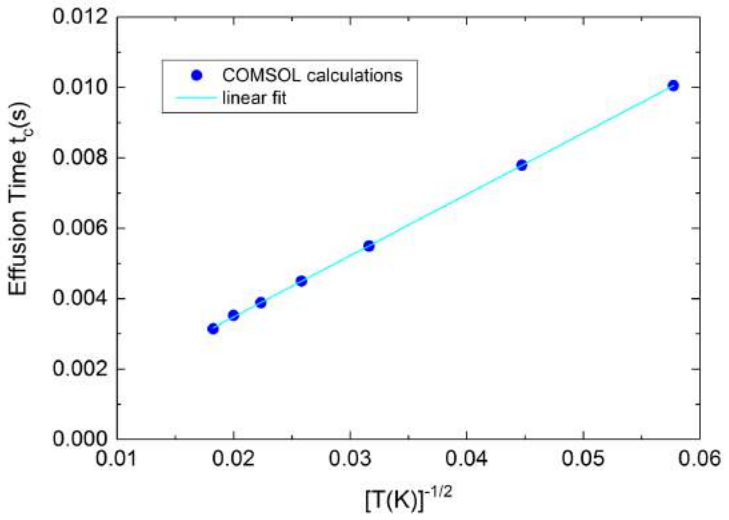

Figure 4-17. Calculated effusion time through a cylindrical tube of R = 2.93 mm and L = 126 mm as a function of $T^{-1/2}$ for Ne particles.

4.5.2 Effusion Simulations and Results

We investigated various stopper geometries and vapor transport configurations, including target and ion source systems used in ISOL facilities. Surface sticking is not included for these studies. Figure 4-18 shows the effusion models which include vapor-transfer tubes with the dimensions of those used in the ISOL targets at TRIUMF ISAC, CERN ISOLDE, and ORNL HRIBF, respectively. The models include a stopper (three stopper disks of ϕ32 x 0.4 mm in a holder of ϕ40 x 15.2 mm) and a hot-cavity ion source (ϕ3 x 30 mm cavity). The transfer tube of the ISAC configuration serves as the ion source itself. The calculated effusion time t_c and average number of wall collisions of these models with and without the ion source are given in Table 4-5. The results indicate that the performance of the three vapor transport systems with the ion source is similar. Furthermore, the effusion time is limited by the small cavity ion source.

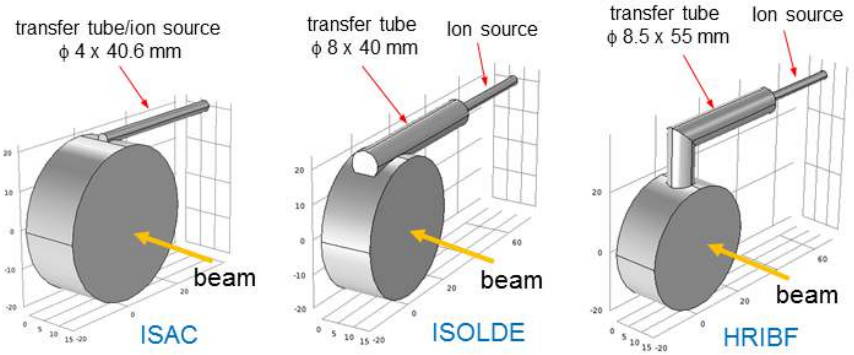

Figure 4-18. Stopper models constructed in COMSOL for the vapor-transport systems used at ISAC, ISOLDE, and HRIBF. The direction of the bombarding beam is indicated.

Table 4-5. Comparison of effusion times and average number of collisions of Sr atoms at T = 293.15 K in COMSOL stopper models with different vapor-transfer lines.

ISOL System	With ion source		Without ion source	
	t_c (s)	$\langle N_{collisions} \rangle$	t_c (s)	$\langle N_{collisions} \rangle$
ISAC	0.508(23)	14861		
ISOLDE	0.551(19)	16086	0.0725(23)	2081
HRIBF	0.515(20)	15224	0.0866(24)	2485

It has been observed [12] that the calculated effusion times with the models that include an ion source are larger than the experimentally measured effusion times. This difference has been explained by the ion extraction effect: once the particles are ionized in the ion source, the ions can be immediately extracted out of the ion source, rather than effuse through the entire length of the ion source. Thus, effusion models that do not include the ionization and ion extraction effect may give unrealistically long effusion times. For this reason, we have excluded the ion source volume in our effusion studies. Instead, we include a 3-mm diameter exit aperture at the end of the transfer tube to represent a realistic coupling to an ion source.

We used COMSOL to investigate over 20 custom stopper and vapor-transport configurations and studied different geometries, numbers of stopper disks, spacing between the disks, and disk arrangements. We present the properties of effusion delays gleaned from those studies.

4.5.2.1 Effusion dependence on volume and conductance

We found that the effusion time t_c is determined by the effusion volume and the conductance of the stopper and vapor transport system. Specifically, we found that the effusion time t_c is linearly proportional to the effusion volume and inversely proportional to the conductance. Figure 4-19 shows the effusion time from our simulations as a function of the effusion volume, where the effusion volume V_{eff} is defined as $V_{eff} = V - V_{disk}$, with V being the total volume of the system and V_{disk} the total volume of the stopper disks. In this plot, each data point represents a simulation of a system with a different volume via changes in the geometries of the stopper holder, transfer tube, and stopper disks.

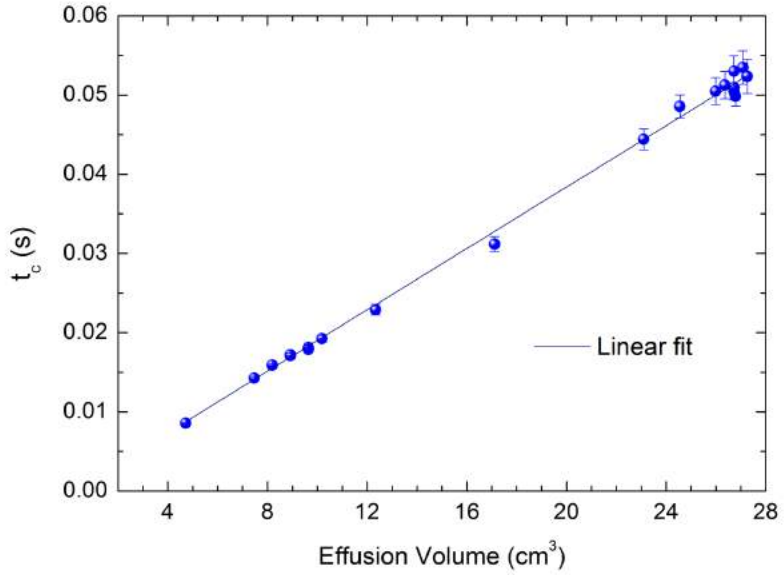

Figure 4-19.Effusion time verses effusion volume for simulations of different configuration systems, using Sr particles at a temperature T = 1000 K.

This observation agrees with the kinetic theory of gases that the characteristic particle evacuation time from an arbitrary geometry system under molecular flow condition, assuming no surface sticking, is given by [6,29]

$$N(t) = N_0 \exp\left(-\frac{t}{\tau_c}\right) \tag{21}$$

$$\tau_c = \frac{V}{C} \tag{22}$$

where N_0 is the initial number of particles at $t = 0$, V is the volume and C is the conductance of the system. The relationship of Eq. (22) is illustrated in the following results as shown in Figure 4-20, obtained by changing the transfer-tube radius while the stopper geometry is fixed. The effusion time is large for a small transfer-tube radius of r = 2 mm, and decreases as r increases, reaches a minimum value at around r = 5 mm, and then increases again at r = 6 mm. This can be explained using Eq. (22): as r increases from 2 mm to 5 mm t_c decreases due to the dominance of increase in conductance, while for r > 5 mm, the volume increase becomes dominant and results in a larger t_c.

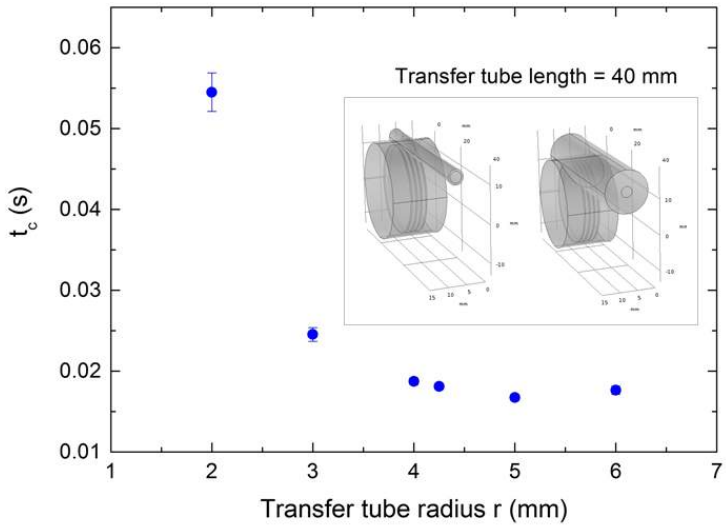

Figure 4-20. Effusion time verses transfer tube radius with fixed transfer tube length and stopper holder geometry, for Sr particles at temperature T = 1000 K.

4.5.2.2 Effusion dependence on number of stopper disks

For a fixed stopper geometry, we found that the effusion time decreases with increasing number of stopper disks. This is consistent with the above observation since the effusion volume is reduced with additional stopper disks (Figure 4-21a). On the other hand, the average number of surface collisions per particle increases with more stopper disks (Figure 4-21b). Consequently, if surface sticking time is not trivial, the total delay time (effusion + surface sticking) will be longer with additional stopper disks.

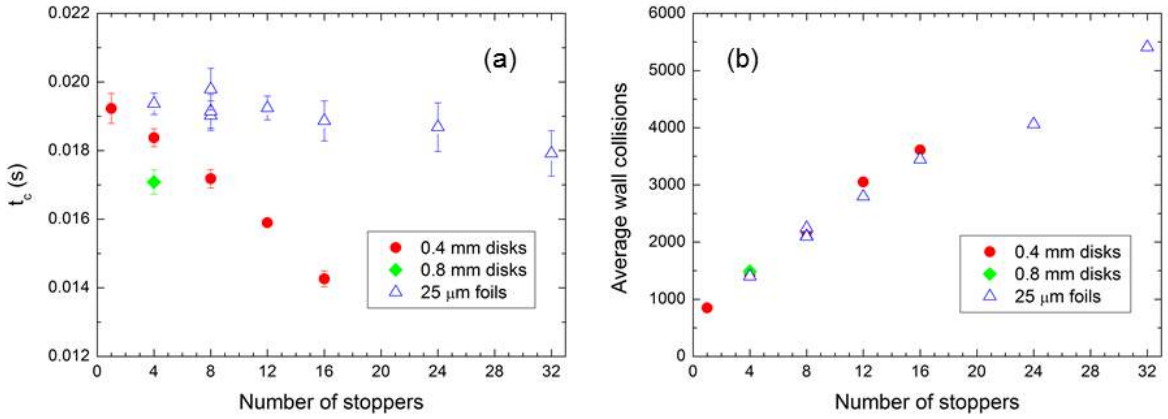

Figure 4-21.(a) Effusion time and (b) average number of wall collisions versus number of stopper disks for the configuration model in Figure 4.8 for Sr particles at temperature T = 1000 K. The stopper disks/foils have dimensions ϕ24 mm and thicknesses 0.4, 0.8, and 0.025mm; the stopper holder dimensions ϕ26 x 15.2 mm; and the transfer tube is ϕ8.5 x 40 mm.

4.5.2.3 Effusion dependence on disk and release location and orientation

For a fixed number of stopper disks, we found that the effusion time is found to be independent of the spacing of the disks, the release location of the particles, and the position and orientation of the disks. Table 4-6 gives a sample of our results, specifically the effusion times of two stopper geometries with 4 stopper disks and different disk spacing. The calculations assume that disks are equally spaced, and that particles are released from one disk surface while the spacing between the disks is changed. As shown, for each geometry, the value of t_c as well as the average number of wall collisions, agree within uncertainties for a wide range of disk spacings.

Table 4-6. Effusion time vs stopper disk spacing for Sr particles at temperature T = 1000 K.

Spacing (mm)	Stopper Disk	Stopper Holder	t_c (s)	Avg. Collisions
0.5	ϕ24 x 0.4 mm	ϕ26 x 15.2 mm	0.0184 (3)	1433
1			0.0181 (3)	1394
2			0.0175 (6)	1365
3			0.0178 (5)	1386
0.1	ϕ32 x 0.4 mm	ϕ30 x 35.56 mm	0.0507 (16)	1764
0.6			0.0507 (17)	1817
1			0.0498(17)	1850
5			0.0502 (20)	1897
10			0.0492 (19)	1841

Table 4-7 gives the effusion times corresponding to different particle releasing positions in a stopper with 16 stopper disks of 0.4 mm thick. The calculations assume that the particles are released from one of the 32 disk surfaces (#1 - #32). The t_c values as well as the average number of surface collisions obtained with different releasing surfaces agree within the statistical uncertainty (one standard deviation).

Table 4-7. Effusion time vs particle release position for Sr particles at temperature T = 1000 K.

Release surface	t_c (s)	Avg. collisions
#1	0.0146(4)	3316
#5	0.0147(2)	3369
#10	0.0145(2)	3357
#16	0.0141(3)	3296
#22	0.0142(3)	3273
#27	0.0143(3)	3315
#31	0.0143(4)	3311

Figure 4-22 shows three models with different stopper disk configurations: (I) stopper disks tilted in the same direction, (II) disks tilted to form a V-shape with the opening toward the transfer tube, and (III) no tilt of the disks. Particles are released from one of the 8 disk surfaces (#1 to #8 from left to right). The effusion times corresponding to particles released from different disk surfaces, especially the surface facing the transfer tube (I: #8, II: #4) and the surface facing away from the transfer tube (#1 for I and II), are compared in Table 4-8. As shown, (II) and (III) configurations have nearly the same t_c values, while (I) may have a slightly smaller t_c if particles are released from #8 surface that facing the transfer tube than from #1 surface (with agreement within 3 standard deviations).

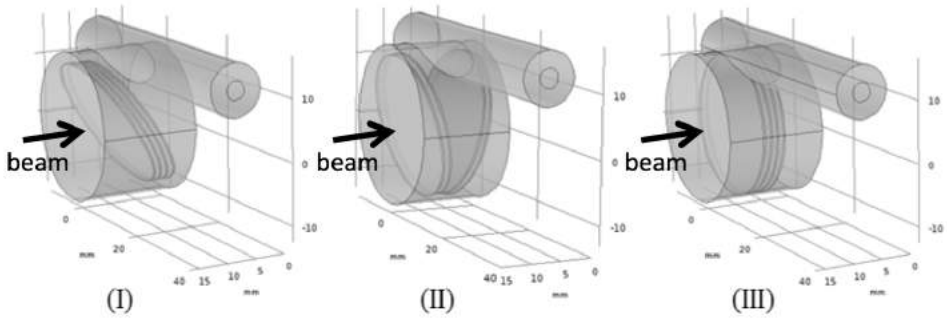

Figure 4-22.Effusion models with different stopper disk configurations: (I) tilted at 30 degrees to the beam axis; (II) tilted to form a V–shape; (III) normal to the beam axis.

Table 4-8. Effusion times of different stopper disk configurations in Figure 4-22, with four stopper disks of 0.4 mm thick. Sr particles are released from one of the 8 disk surfaces at temperature T = 1000 K.

configuration	Release surface	t_c (s)	Avg. collisions
I	#8	0.0167(6)	1148
	#1	0.0187(2)	1250
II	#4	0.0174(4)	1316
	#1	0.0178(5)	1386
III	#4	0.0176(5)	1331
	#1	0.0179(4)	1307

4.5.2.4 Summary of effusion results

Based on the above results, we conclude that the solid stopper system should have these characteristics for fastest effusion release (*i.e.*, shortest effusion delay time):

- use as few stopper disks as possible;
- have a small total volume;
- have a high gas conductance;

Furthermore, as noted above, we find that effusive release times are independent of the spacing, position, and orientation of the stopper disks.

4.5.3 Comparing effusion in different vapor-transport configurations

We studied effusion through a variety of different vapor-transport configurations, as illustrated in Figure 4-23. Among these, S2 and S3 are the transfer line configurations used at the ISOLDE and SPES facilities, respectively, and H1 - H3 have more open geometries for high vapor conductance as proposed by Zhang and Alton[12].

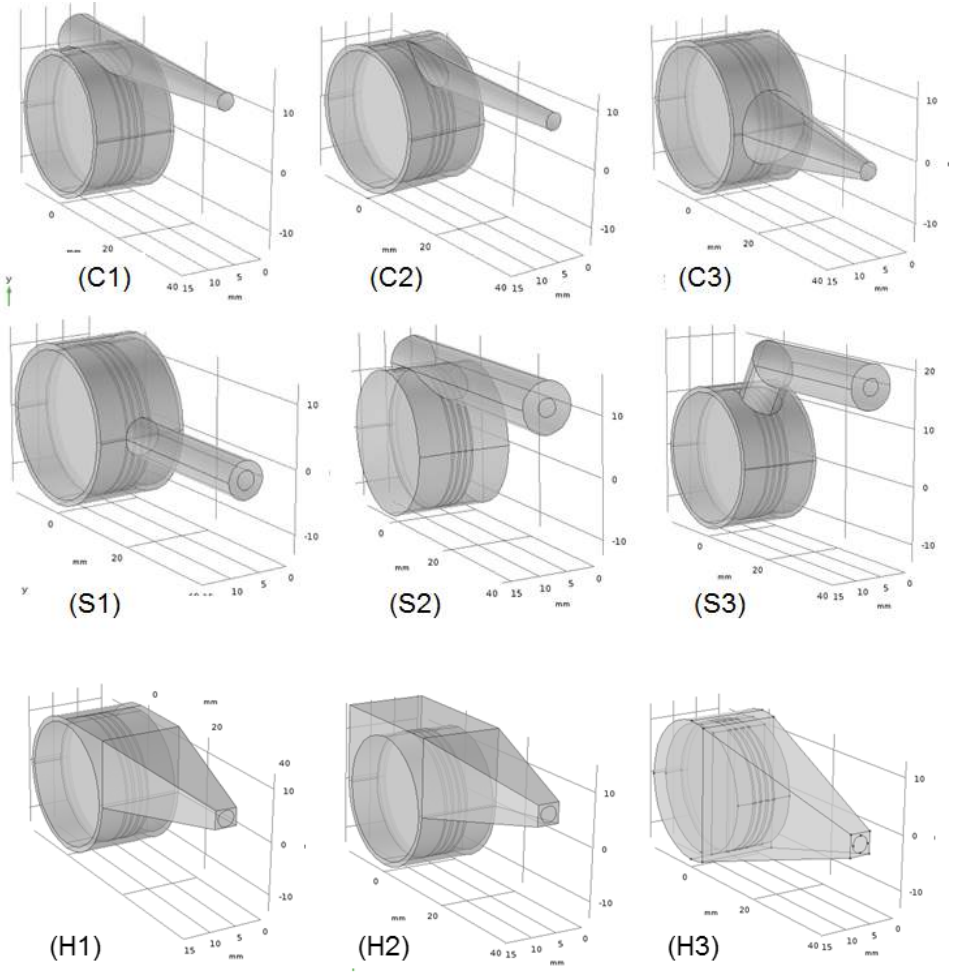

Figure 4-23. Some of the vapor-transport configurations studied: (C1-C3) tapered transfer-tube; (S1-S3) straight transfer-tube; (H1-H3) high-conductance transport.

To compare these vapor transfer systems, we considered the same stopper holder and stopper disks and assumed that particles are released from the same disk surface and exit the transfer line through a 3-mm diameter aperture. In addition, the distance from the center of the stopper holder to the end of the transfer line was set to be 40 mm for all models. The calculated effusion times at different transfer tube radius for C and S models indicate, as shown in Figure 4-24, that straight transfer tube systems (S models) are faster than the conical tapered transfer tube systems (C models). S models have a minimal t_c for $r0$ = 5 mm, and configuration S1 has the fastest effusion release among these models.

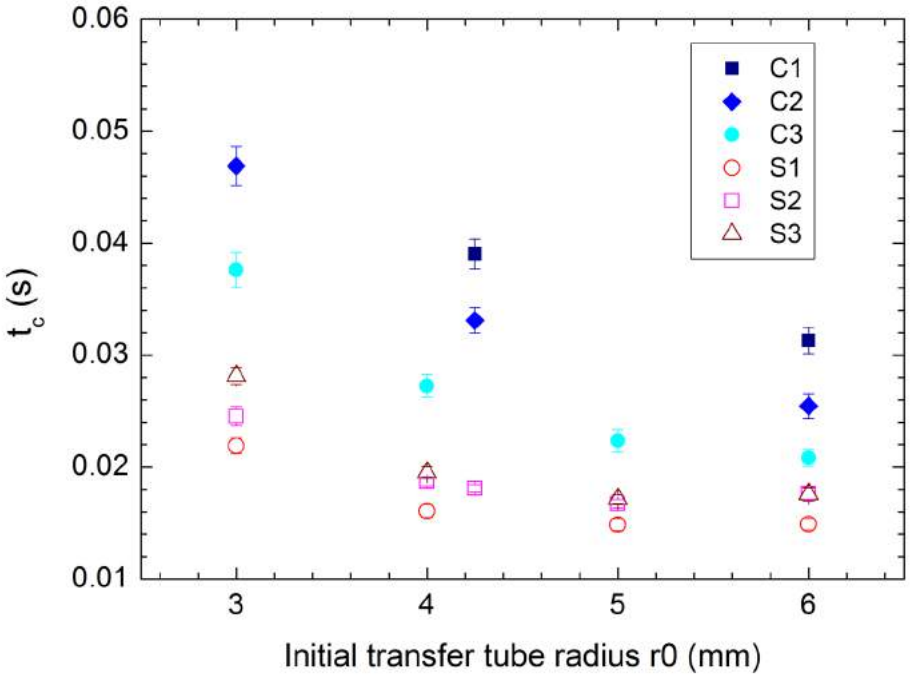

Figure 4-24.Comparison of the effusion times of group C and group S models for different transfer tube radii. For group C, the transfer tube is tapered from the initial radius r0 to the exit aperture of r = 1.5 mm at the end of the transfer line. For group S, r0 is the transfer tube radius. The simulations are for Sr particles and temperature T = 1000 K.

The effusion times of the high-conductance models (H group) are given in Table 4-9, which are larger than the minimal t_c of the S1 model with transfer tube $r0$ = 5 mm. This is because that although the H models have high-conductance for vapor transfer, they also have a relatively larger overall volume, and the overall effect yields a longer effusion time than the S models.

Table 4-9. Effusion times of group H models, together with the minimal effusion time of the S1 model. The simulations are for Sr particles at temperature T = 1000 K.

Model	t_c (s)	Avg. collisions
H1	0.0174(6)	1235
H2	0.0192(2)	1229
H3	0.0169(6)	1178
S1 (r0 = 5 mm)	0.0148(5)	1146

In above simulations, the transfer tube length is fixed to be 40 mm from the center of the stopper holder. A shorter transfer tube should further reduce the effusion time. We found that as the transfer tube length is shortened towards zero, the effusion time of the C3 configuration decreases more rapidly and eventually becomes comparable or smaller than that of the S1 configuration, as shown in Figure 4-25. It is also seen that for both models, t_c has a minimal value and increases again for a tube shorter than 3 mm and for the simulation without the transfer tube. The minimal t_c of the C3 model may be slightly smaller than that of the S1 model, but the difference is small. Based on these studies, we selected both S1 and C3 with a short transport tube of 3-5 mm as candidate vapor-transport configurations for a proof-of-concept stopper system. An extensive study of these configurations is given in Section 7 below.

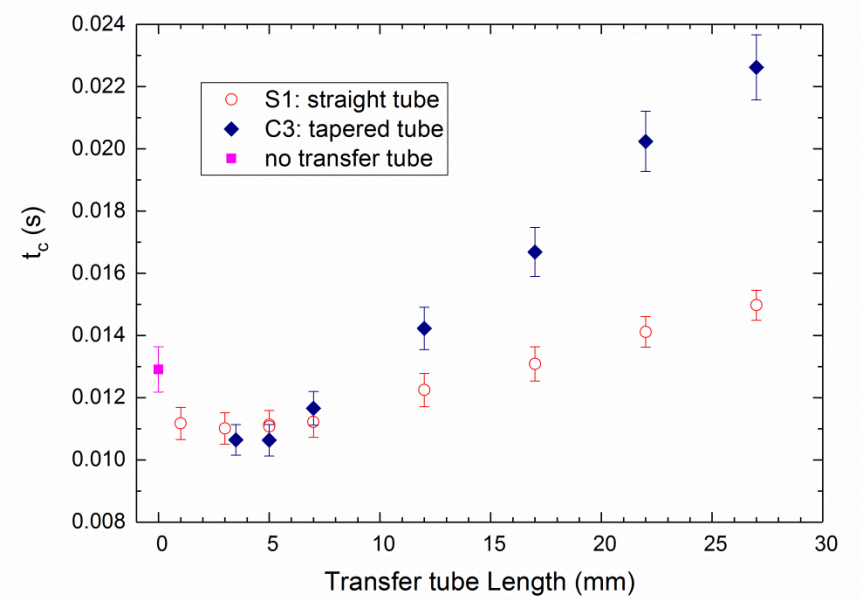

Figure 4-25. Comparison of the effusion times of the S1 and C3 configuration at different transfer tube lengths. For S1, the transfer tube radius is r = 5 mm; for C3, the transfer tube is tapered from radius r0 = 5 mm to r = 1.5 mm of the exit aperture. The simulations are for Sr particles and T = 1000 K.

5. STOPPER THICKNESS

In a solid stopper material, the stopped fragment ions are distributed over a finite range. Tables 5-1 and 5-2 show the estimated mean ion stopping range and longitudinal range straggling, which is the standard deviation of the mean, for the beams of interest in Ta and graphite stoppers, respectively. The beam energies in these tables are estimated maximum fragment energies at FRIB [20]. For fast diffusion and effusion release, the stopper thickness should be minimized to allow thinner stopping foils and at the same time a minimal number of foils to be used. This could be achieved by slowing down the fragment beams with proper degraders before the stopper such that all the fragment ions can be implanted into the stopper material over a depth that matches the width of the range straggling. According to LISE++ stopping

simulations, the stopped fragment ions will have a Gaussian range distribution along the beam axis. Thus, the minimal stopper thickness could be three or four times of the standard deviation of the mean range , which can capture 99.73% or 99.99% of the stopped ions, respectively. The last column in these tables gives the 3-sigma thickness for the indicated beam energies.

Table 5-1. Estimated mean ion stopping range and the range straggling (standard deviation) in Ta, calculated with SRIM, and proposed stopper thickness for each beam.

Beam	Z	A	E (MeV/u)	Projected Range (mm)	Longitudinal Straggling (μm)	Stopper Thickness 3-sigma (μm)
Li	3	7	251.3	34.75	1280	3840
Be	4	9	248.4	25.58	1030	3090
Ne	10	20	237.7	8.25	758.9	2277
Na	11	23	241.5	7.84	313.9	942
Mg	12	24	238.8	6.95	271.7	815
Ar	18	40	216.5	4.2	122.7	368
K	19	39	227.5	4.19	174.0	522
Ca	20	40	226.1	3.82	161.8	485
Kr	36	84	186.1	1.85	51.8	155
Rb	37	85	187.3	1.8	65.4	196
Sr	38	88	187.2	1.78	63.0	189
Xe	54	132	175.6	1.21	16.8	50
Cs	55	133	166.7	1.08	39.5	119
Ba	56	138	166.7	1.11	41.2	124
Rn	86	222	158.8	0.799	8.8	26
Fr	87	223	158.5	0.791	27.5	83
Ra	88	226	158.5	0.790	27.0	81

Table 5-2. Estimated mean ion stopping range and the range straggling (standard deviation) in graphite, calculated with SRIM, and proposed stopper thickness for each beam.

Beam	Z	A	E (MeV/u)	Projected Range (mm)	Longitudinal Straggling (μm)	Stopper Thickness 3-sigma (μm)
Li	3	7	251.3	147.68	5270	15810
Be	4	9	248.4	108.35	4330	12990
Ne	10	20	237.7	34.79	1340	4020
Na	11	23	241.5	33.11	1330	3990
Mg	12	24	238.8	29.33	1150	3450
Ar	18	40	216.5	17.61	720.7	2162
K	19	39	227.5	17.62	739.7	2219
Ca	20	40	226.1	16.05	688.2	2065
Kr	36	84	186.1	7.64	280.0	840
Rb	37	85	187.3	7.46	274.6	824
Sr	38	88	187.2	7.35	264.2	793
Xe	54	132	175.6	4.96	188.9	567
Cs	55	133	166.7	4.4	165.5	497
Ba	56	138	166.7	4.52	172.7	518
Rn	86	222	158.8	3.23	116.4	349
Fr	87	223	158.5	3.19	114.5	344
Ra	88	226	158.5	3.19	112.7	338

6. COUPLED BEAM HEATING, DIFFUSION, AND EFFUSION SIMULATIONS

The above effusion simulations have assumed a constant temperature in the stopper system. In reality, the stopper may have large temperature variations due to stopped beam heating (Section 4.2). With COMSOL Multiphysics, we addressed this by developing a model that couples beam heating and effusion effects where particle effusion (including surface sticking) can be calculated with realistic beam-heated temperature distributions in the stopper system. An example of the coupled simulations is presented here, with details of each step given in the subsections below.

6.1 SYSTEM GEOMETRY

The geometry of the coupled model, consisting of a set of stopper foils inside a holder with an entrance window and endcap, a vapor transfer tube, and an ion source, is shown in Figure 6-1. As an example of selecting the thickness of the foils and the entrance window we considered a monoenergetic ^{88}Sr beam particles with 187 MeV/u energy. The SRIM estimate of their mean stopping range and the range straggling in Ta are given in Table 5-1 as 1.78 mm and 63 μm, respectively. Plotting out the stopping power as a function of distance, Figure 6-2, suggests an arrangement of a 1.65 mm-thick Ta entrance window followed

by four 50 μm-thick Ta stopper foils. Figure 6-3 shows the LISE++ calculation of the stopped ion distribution along the beam axis in the Ta foils for this arrangement; the distribution is a Gaussian centered around 0.11 mm with a FWHM of about 63 μm. Almost all the Sr ions are captured in the four foils. For the LISE++ calculation, the projectile beam is assumed to have a relative momentum spread of 0.5% and the results agree with the SRIM estimation. Under realistic experimental conditions where beam energies can drift or be tuned incorrectly, or the fragment beam momentum spread is larger, it would be necessary to slightly increase the stopper foil thickness to account for these effects. For this example, the Ta window is used as the energy degrader. In practice, adjustable energy degraders should be used according to beam energies. Moreover, monoenergetic degraders [31, 32] are widely used to compress the range distribution of fragments ions for injection into gas stoppers. The same range compression technique should be employed for solid stoppers to minimize the stopper thickness. We used 50 μm-thick stopper foils in this example to demonstrate coupled thermal-effusion simulations. For real stoppers, thinner foils are desired for faster diffusion release. The optimal foil thickness and number of foils will depend on the diffusion and effusion properties of the fragment species.

The 50-μm thick Ta foils are chosen to have a radius r = 16 mm and are held inside a Ta cylindrical holder (r = 20 mm and L = 20 mm, 1 mm wall thickness). We chose a Ta vapor transport line similar to that used at ISOLDE (Figure 4-18) (r = 4.25 mm, L = 40 mm, 0.5 mm thick wall), and an ion source that is a cylindrical cavity (r = 1.5 mm, L = 30 mm, 1 mm thick wall) representing sources widely used for ISOL surface ionization sources and laser ion sources.

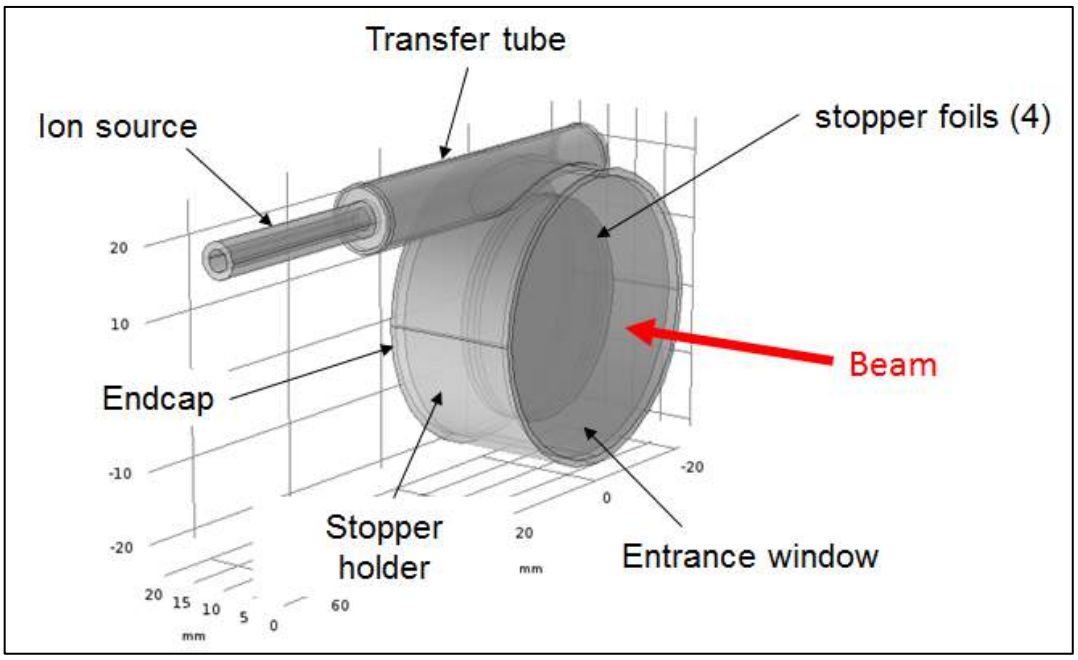

Figure 6-1.Geometry of the stopper model for thermal simulation: four Ta stopper foils in a cylindrical holder with an entrance window and endcap, connected to a hot-cavity ion source via a transfer tube. The bombarding beam enters the system as indicated.

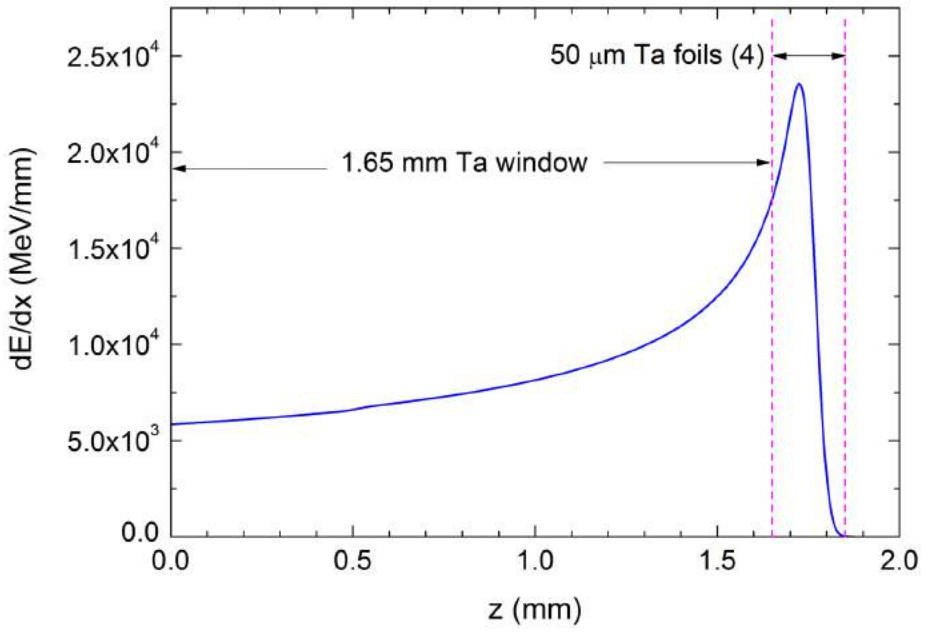

Figure 6-2. Stopping power of 187 MeV/u ^{88}Sr beam in Ta as a function of depth obtained with LISE++ in a stopper configuration of a 1.65 mm Ta window followed by four 50 μm -thick Ta foils.

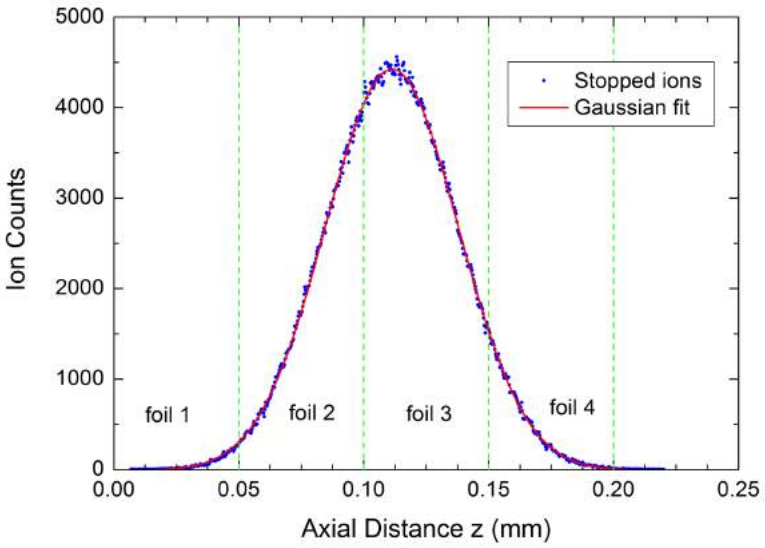

Figure 6-3. Axial distribution of the stopped ^{88}Sr ions in the four Ta foils after passing through the 1.65mm-thick Ta entrance window, as calculated with LISE++. Foil 1 is the first foil encountered by the Sr beam after passing through the Ta window; almost all particles stop before exiting Foil 4.

6.2 THERMAL SIMULATION AND TEMPERATURE DISTRIBUTIONS

Steady state heat transfer simulations were performed using the stopping power (Figure 6-2) in the Ta window and the foils as the heat source to provide the equilibrium temperature distributions in the stopper holder, stopper foils, the transfer tube, and the cavity ion source for various Sr beam intensities. An example of the temperature distribution of the stopper system with 10 nA Sr beam heating is given in Figure 6-4. The detailed temperature distributions in the four Ta foils are shown in Figure 6-5.

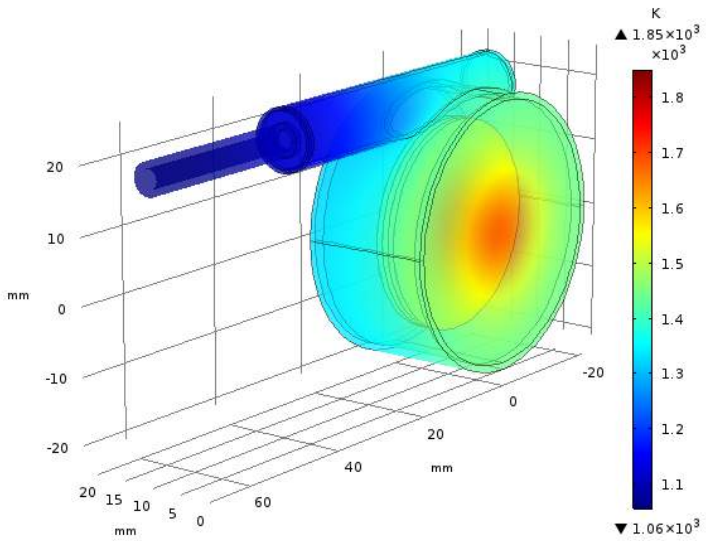

Figure 6-4 . Equilibrium temperature distribution of the stopper and ion source system heated by a 187 MeV/u 88Sr beam with 10 nA intensity. Maximum and minimum temperatures are 1850 K and 1060K, respectively, with an average of 1455 K.

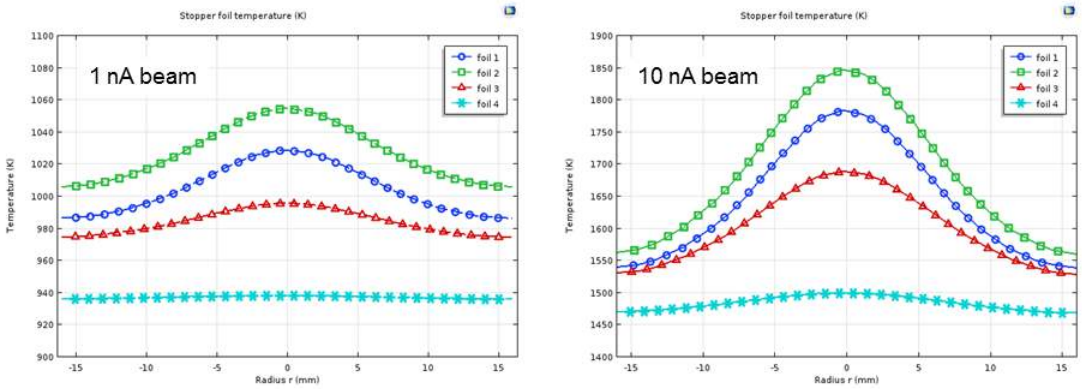

Figure 6-5.Temperatures in radial direction in the Ta foils heated by Sr beams of intensity 1 nA (left) and 10 nA (right). Foil 1 is the first foil that the beam encounters after passing through the Ta window. The temperature distributions in the foils are radially symmetric. Simulations with a 10 nA Sr beam result in temperatures that are ~ 1.8 times higher than those with a 1 nA beam. Note the different vertical scales in the two plots.

6.3 COUPLING EFFUSION SIMULATIONS WITH BEAM-HEATING TEMPERATURE DISTRIBUTIONS

For reasons discussed in Section 4.5.2, the ion source was not included in our effusion simulations, which began with 10,000 Sr atoms being released from one of the foil surfaces into the vacuum at time t = 0 with a Gaussian spatial distribution on the foil surface (Figure 6-6). The initial particle temperatures were determined by the foil temperature distribution from the steady state heat transfer simulation, as shown in Figure 6-7. The Sr atom movements were traced as they bounced between the walls of the solid materials. As discussed in Section 4.5, the Sr atoms were assumed to be thermalized with the surface at each wall collision and were reemitted according to Knudsen cosine law with a Maxwell-Boltzmann velocity distribution. The Sr particle temperatures at t = 0.001 s after releasing are displayed in Figure 6-8, showing particles thermalizing with the walls.

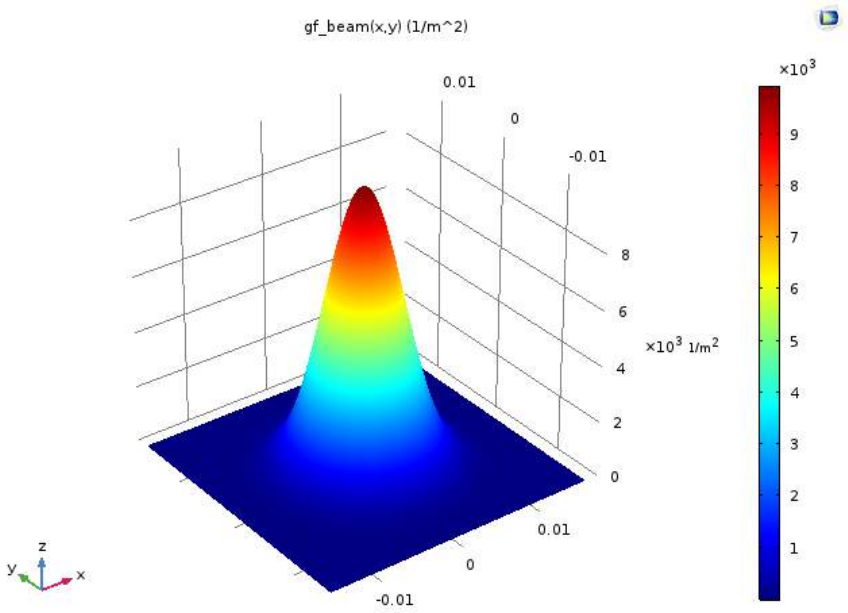

Figure 6-6. Spatial distribution of Sr atoms on the release surface, corresponding to a Gaussian distribution of beam particles with FWHM = 9.42 mm; x- and y-axes units: m. The Ta foil radius was chosen to be the 4-sigma width (16 mm) of the beam distribution.

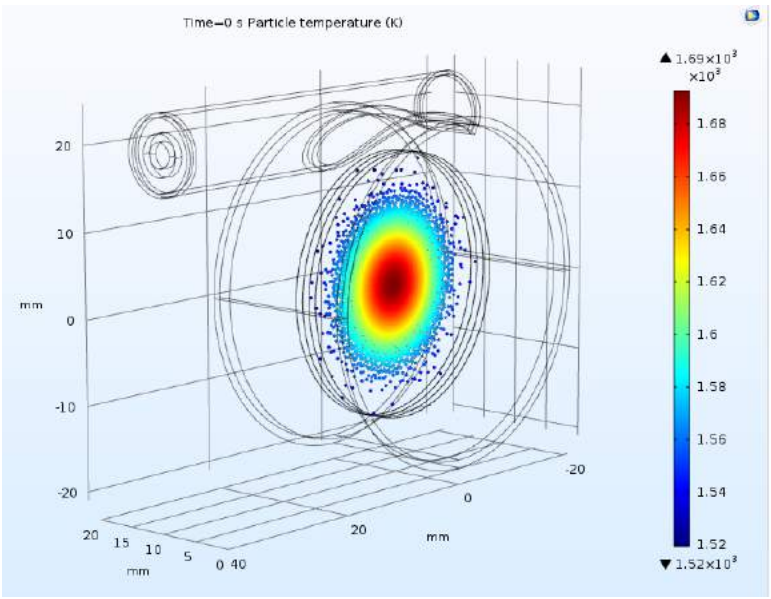

Figure 6-7. Initial Sr atom temperatures on the release surface (the surface of the 3rd foil) for the case with a 10 nA incident Sr beam current. The temperature distribution of this foil is shown in Figure 6-5 (right).

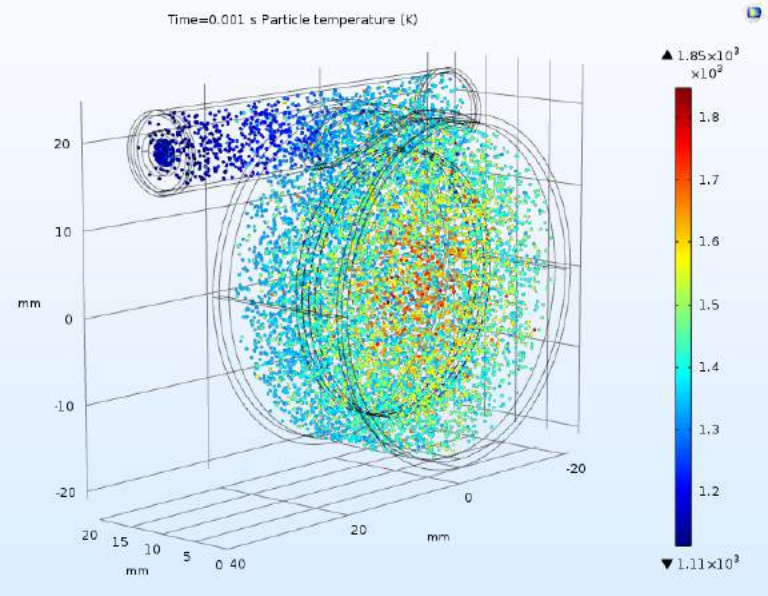

Figure 6-8. Sr atom temperatures at t = 0.001 s after release for the case with a 10 nA incident Sr beam current. This also shows the temperature distribution of the system, with maximum and minimum temperatures of 1850 K and 1110 K, respectively.

6.4 SURFACE STICKING TIME

The surface sticking time at each wall collision was calculated using Eq. (19) in Section 4.5 and summed to give the total sticking time when a particle exits the stopper system. This sticking time, which depends on the activation energy for desorption, E_a, was added to the particle travel time to exit the system to give the total time in the stopper for each particle. E_a values range from 0.25 eV to 2.5 eV, where E_a = 0.25 eV represents pure physical adsorption conditions where the attraction between the adsorbates and the surface arises from weak van der Waals forces. This is usually the case for noble gas elements [15]. Larger E_a values would correspond to the presence of chemisorption and will lead to longer surface sticking times. Figure 6-9 shows the particle effusion transmissions as a function of time with and without surface sticking. The calculated overall effusion times (t_c) corresponding to different E_a values and with two stopped beam intensities are given in Table 6-1. In the presence of surface sticking, it was seen that the overall effusion time is significantly shorter with 10 nA beam heating than 1 nA beam, because of the higher temperatures of the system surfaces caused by the more intense 10 nA beam (Figure 6-5). This clearly shows the importance to operate the stopper at temperatures as high as practically achievable. This principle should be added to the geometrical design considerations found above in Section 4.5.2.4.

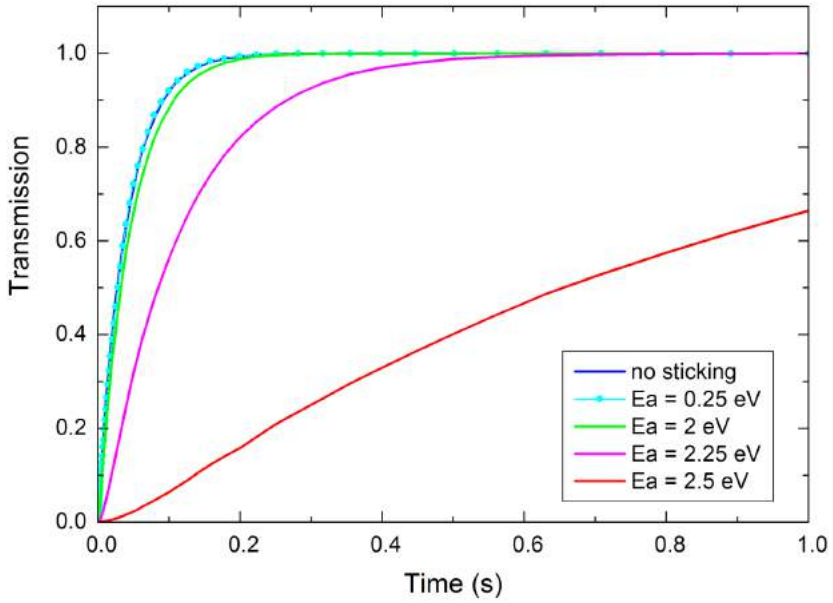

Figure 6-9. Effusion transmission of Sr atoms from the stopper system heated by 10 nA Sr beam with different activation energies of adsorption E_a.

Table 6-1. Calculated overall effusion times for different activation energies of desorption E_a, with 10 nA and 1 nA stopped Sr beam intensities. The temperature distribution of the stopper system is shown in Fig. 6-8.

E_a (eV)	t_c (s) (10 nA beam)	t_c (s) (1 nA beam)	Avg. collisions
No sticking	0.040(1)	0.050(1)	2072
0.25	0.040(1)	0.049(1)	
1.0	0.040(1)	0.050(1)	
1.5	0.041(1)	0.010(1)	
1.75	0.041(1)	1.33(4)	
2.0	0.048(1)	36(2)	
2.25	0.12(1)	965(37)	
2.5	0.93(3)	2.76E+4	
3.0	118(2)	2.23E+7	

6.5 COMPARISON OF COUPLED AND NON-COUPLED EFFUSION SIMULATIONS

To our knowledge, our coupled thermal-effusion simulation is the first for such systems. Previously, effusion simulations have been performed under the assumption of a constant temperature for the whole system. For comparison, we also performed non-coupled effusion simulations for the stopper system described above. From the steady state heat transfer simulations for an incident 10 nA Sr beam intensity (Section 6.2), the average temperature of the stopper system is found to be 1445 K (Figure 6-4) and that of

the stopper foils is 1608 K (Figure 6-5, right). We therefore carried out non-coupled effusion simulations at two constant temperatures, T_avg = 1400 K and 1650 K, that are representative of the different components within the system. We determined the effusion time including the surface sticking effect, for these two average temperatures and for different values of the activation energy for desorption E_a. The results of the non-coupled (*i.e.*, constant-temperature) simulations are compared to the coupled thermal-effusion simulations (Table 6-1, Column 2) in Figure 6-10. It can be seen that the non-coupled simulations significantly underestimates the effusion release time when surface sticking times are dominant (*i.e.*, when activation energy for desorption E_a values are high). Because of the short lifetimes of some radioactive beam species, this result quantitatively demonstrates that non-coupled simulations can in some cases predict release times that are far less than the actual delay times of the system -- and therefore lead to incorrect conclusions for experimental planning.

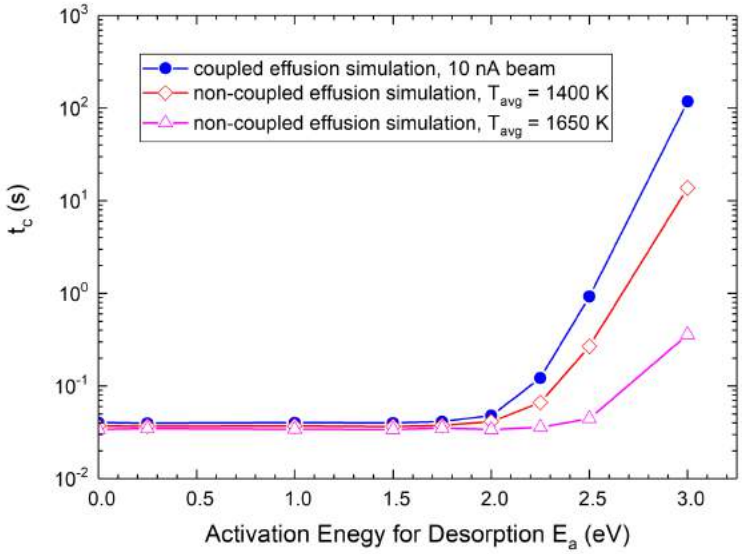

Figure 6-10. Comparison of the calculated effusion time t_c, obtained with coupled and non-coupled effusion simulations for different values of the activation energy for desorption E_a. The temperature distribution for the coupled simulation is shown in Fig. 6-8.

6.6 COMBINING DIFFUSION AND EFFUSION RELEASE TIMES

The diffusion and effusion delays can be combined by convolution:

$$f(t) = \int_0^{t_p} f_e(t) f_d(t_p - t)\, dt \tag{23}$$

where $f(t)$ is the overall release rate as a function of time, $f_d(t)$ is the diffusion release rate as a function of time, and $f_e(t)$ is the effusion release rate as a function of time. For thin stopper foils, $f_d(t)$ is the fractional diffusion release rate given by Eq. (13). The effusion release rate $f_e(t)$ is obtained by taking the histogram of the particle release times from effusion simulations and fitting the data to the following function [10]:

$$f_e(t) = A\left[1 - \exp\left(-\frac{t}{t_1}\right)\right]\exp\left(-\frac{t}{t_2}\right) \tag{24}$$

As depicted in Figure 6-11, the effusion release time distribution can be well represented by Eq. (24).

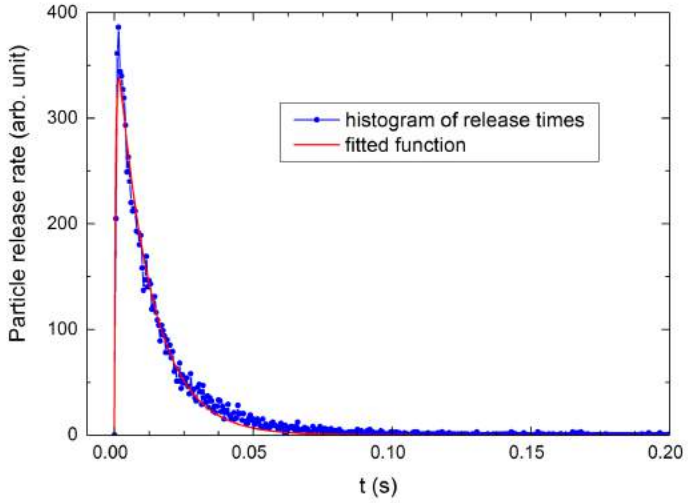

Figure 6-11. Comparison of the effusion release rate and the fit to the formula in Eq. (24).

To calculate the convolution analytically [10, 33], we used the first 50 terms in Eq. (13) for the diffusion function

$$f_d(t) = \frac{8D}{h^2}\sum_{n=0}^{50} exp\left[-\frac{D(2n+1)^2\pi^2}{h^2}t\right] \tag{25}$$

The error introduced by using the approximation in Eq. (25) for the infinite series is about 0.4%. The diffusion coefficients for a number of radioisotopes in various solid materials have been reported to range between 10^{-7} and 10^{-12} cm^2/s at high temperatures of 2150 – 2800 K [33]. As an example, we consider a diffusion coefficient $D = 10^{-7}$ cm^2/s, and plot the overall particle release rates obtained with Eqs. (23) - (25) for different stopper foil thicknesses in Figure 6-12. We note that the value for the diffusion coefficient of Sr in Ta is unknown. As shown in the figure, the individual stopper foils should be as thin as possible (~ a few microns) for reasonably fast diffusion release. This suggests more thinner foils are preferable over fewer thicker foils to minimize diffusive delays. This needs to be balanced with the longer surface sticking time that results from using more foils. For a given required target thickness (as determined from the spatial

distribution of the stopped ion species in the target material at the bombarding energy), the optimal foil thickness and number of foils will depend on the values of the diffusion coefficient D and the activation energy for desorption E_a.

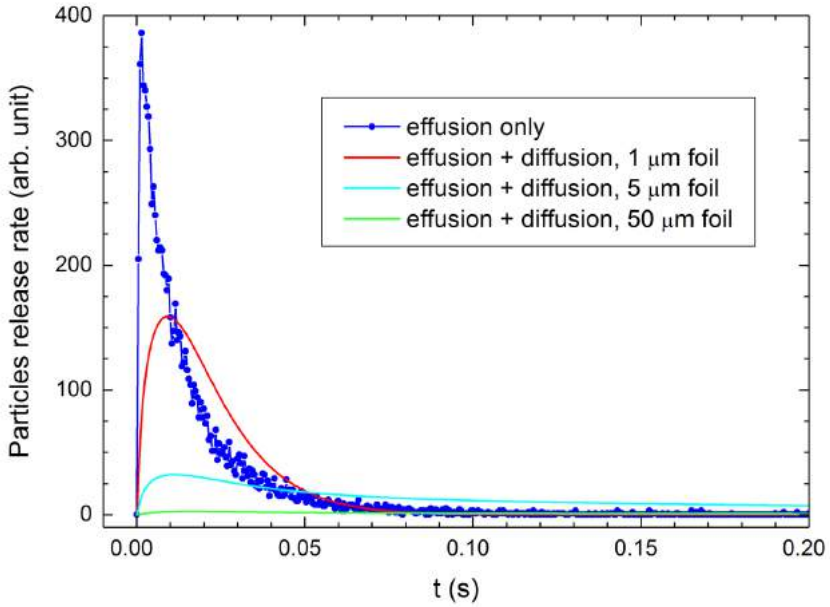

Figure 6-12. Overall particle release rate with diffusion and effusion processes, for a diffusion coefficient D = 10^{-7} cm2/s and stopper foil thicknesses of 1, 5, and 50 μm.

7. PROOF-OF-CONCEPT DESIGN

In this section, we present details of our proof-of-concept (POC) design.

7.1 COUPLED THERMAL-EFFUSION SIMULATIONS

As discussed in Section 4.5.3, the S1 and C3 vapor-transport configurations were selected as candidate vapor-transport configurations for the proof-of-concept (POC) solid stopper based on effusion simulations. Here we present coupled thermal-effusion simulations including surface sticking for a POC design with the C3 tapered vapor-transport tube of length 5 mm. The stopper is the same as that presented in Section 6: four Ta stopper foils of 50 μm thick inside a cylindrical holder with a 1.65 mm-thick Ta entrance window for stopping ^{88}Sr fragment ions of 187 MeV/u and a 1.6 mm Ta endcap. However, for the POC design, the Ta foils have a smaller area, with a radius of r = 12 mm corresponding to 3-sigma of the fragment beam transverse distribution. The stopper holder is also smaller, with r = 13 mm and L = 15.2 mm. Figure 7-1 shows the COMSOL model of the POC stopper connected to a hot-cavity ion source. The equilibrium

temperature distributions in the stopper system and in the four Ta foils are shown in Figures 7-2 and 7-3, respectively.

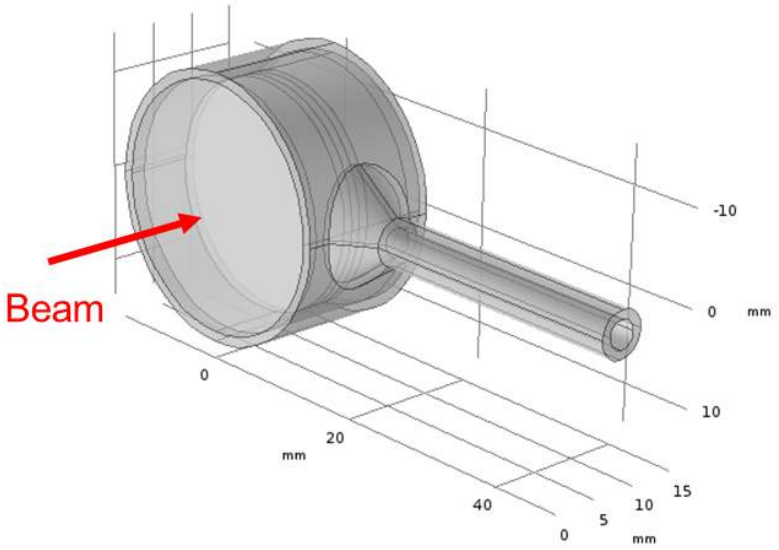

Figure 7-1. Geometry of a POC stopper: four Ta stopper foils in a cylindrical holder connected to a hot-cavity ion source via a short-tapered transfer tube. The fragment beam enters the stopper as indicated.

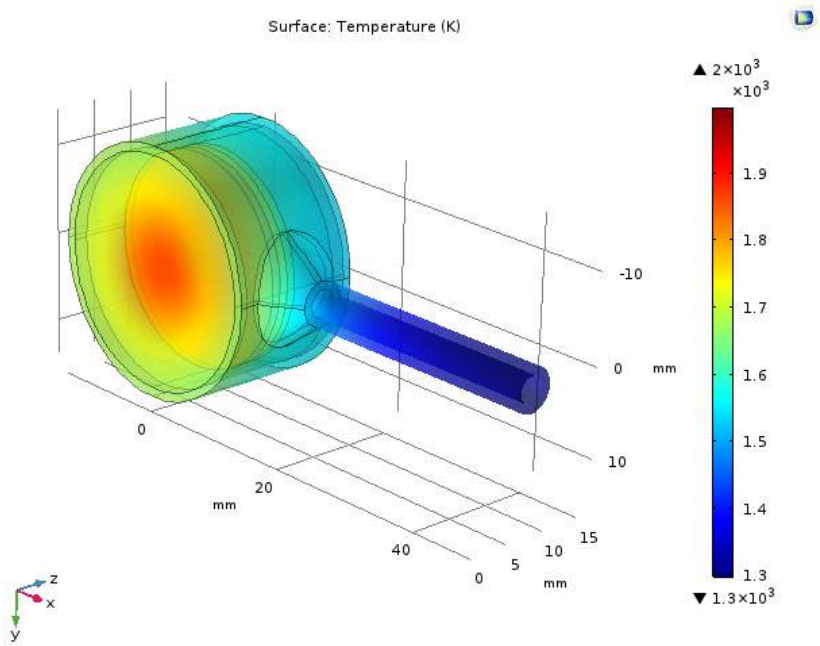

Figure 7-2. Equilibrium temperature distribution of the POC stopper system for stopping a 187 MeV/u beam of ^{88}Sr with an intensity of 10 nA.

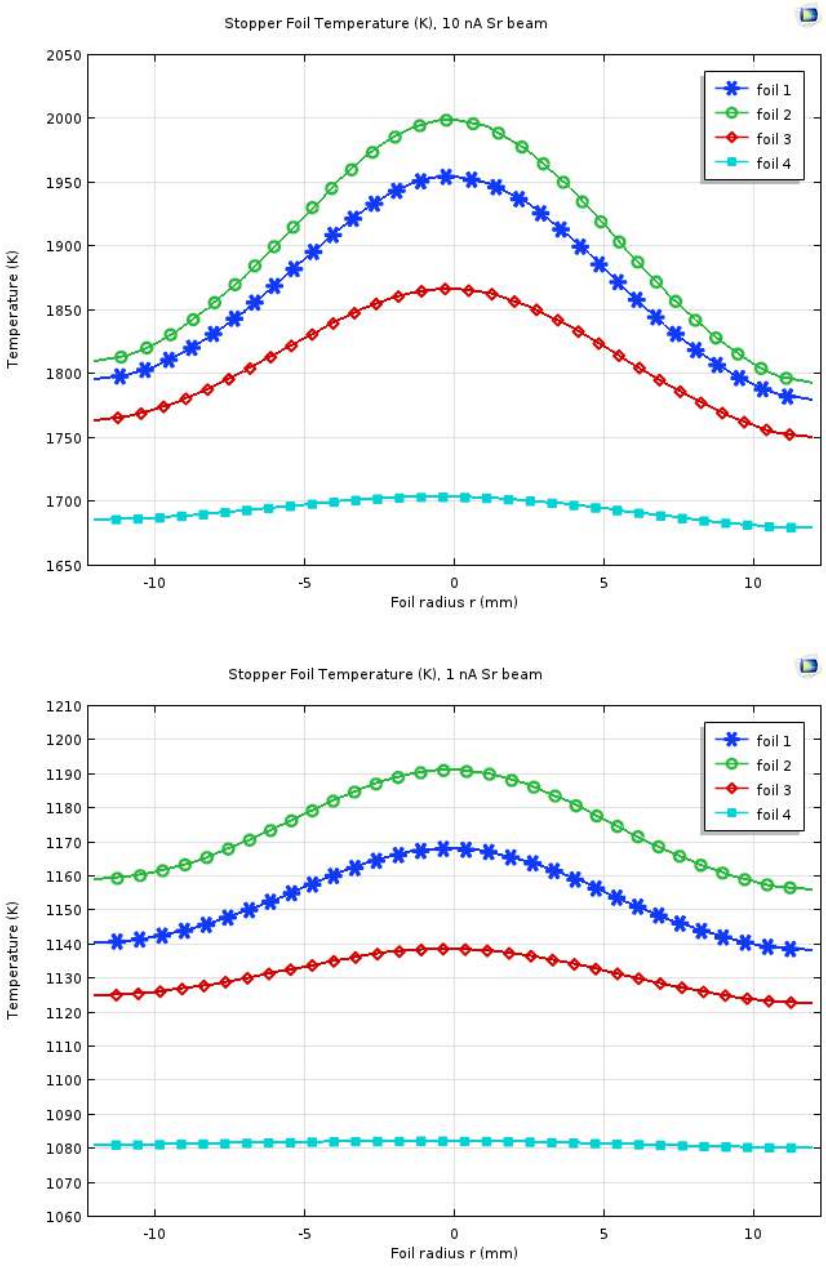

Figure 7-3. Equilibrium temperature distributions in the Ta foils for Sr beams of intensity 10 nA (upper) and 1 nA (lower).

The effusion simulation for the POC stopper is performed without the ion source as shown in Figure 7-4. A total of 10000 Sr atoms were released at t = 0 from both surfaces of the 3rd Ta foil with initial temperatures determined by the foil's equilibrium temperature distribution as plotted in Figure 7-3.

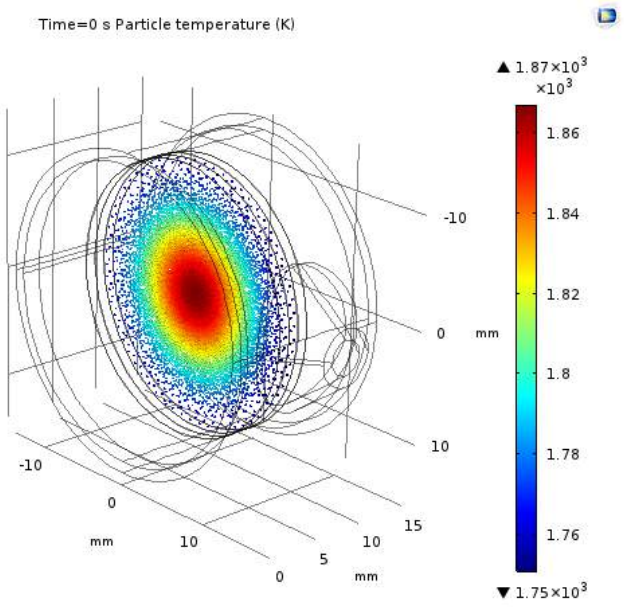

Figure 7-4. Effusion model of the POC stopper, showing the initial temperatures of 10000 Sr atoms on the release surface of the 3rd foil, for the case with an incident Sr beam intensity of 10 nA.

The calculated overall effusion time t_c for 1 nA and 10 nA Sr beam intensities with surface sticking times corresponding to different E_a values are summarized in Table 7-1. Comparing with the stopper model presented in Section 6 (Table 6-1), the POC design gives significantly shorter effusion times, especially when surface sticking is considered. This improvement can mainly be attributed to the reduced overall volume as well as the much smaller average number of surface collisions per particle. As noted again, the effusion time for an activation energy of desorption of E_a = 2.5 eV for a 1 nA beam is orders of magnitude larger than for a 10 nA beam, due to lower temperatures (Figure 7-3).

Table 7-1. Calculated effusion times of the POC stopper for different activation energies of desorption, with 10 nA and 1 nA stopped Sr beam intensities.

E_a (eV)	t_c (s) (10 nA beam)	t_c (s) (1 nA beam)	Avg. collisions
No sticking	0.0082(1)	0.0103(1)	790
0.25	0.0083(1)	0.0103(1)	
1.0	0.0082(1)	0.0104(1)	
1.5	0.0082(1)	0.0114(1)	
1.75	0.0083(1)	0.0268(3)	
2.0	0.0083(1)	0.27(2)	
2.25	0.0086(1)	4.3(1)	
2.5	0.0116(2)	73(2)	
3.0	0.14(2)	18490	

The volume of the POC stopper can be further reduced, which will result in even lower effusion times. We plan to optimize this POC stopper design for eventual construction, installation, commissioning, and utilization to generate unstable reaccelerated beams at FRIB.

7.2 SIMULATIONS WITH REALISTIC EXTERNAL HEATING

In general, external heating will be required to raise the solid stopper to the high temperatures needed for fast diffusion and effusive release. If a hot-cavity ion source is attached to the vapor transport tube, this source will also need to be heated to a high operating temperature (~2000 C). We have incorporated a simple but realistic resistive heating element into our model and included the resulting heat transfer in our simulations. Figure 7-5 shows the COMSOL model for the POC stopper connected to a hot-cavity ion source assembly and a resistive heater bus which also serves to support the stopper. This particular configuration is adapted from the standard ISOLDE surface ionization source assembly with a tubular Ta-cavity (3-mm ID, 30 mm long, 1-mm wall), a Ta support, and a Ta heat shield as shown in the figure. The CAD drawings for the source assembly were provided by Dr. Klaus Wendt's group at Mainz University, imported into the COMSOL 3D model, and adapted for our POC model. The stopper heater bus is a 10-mm wide, 80-mm long, and 2-mm thick bar of Ta. All the parts are assumed have perfect thermal and electrical connections.

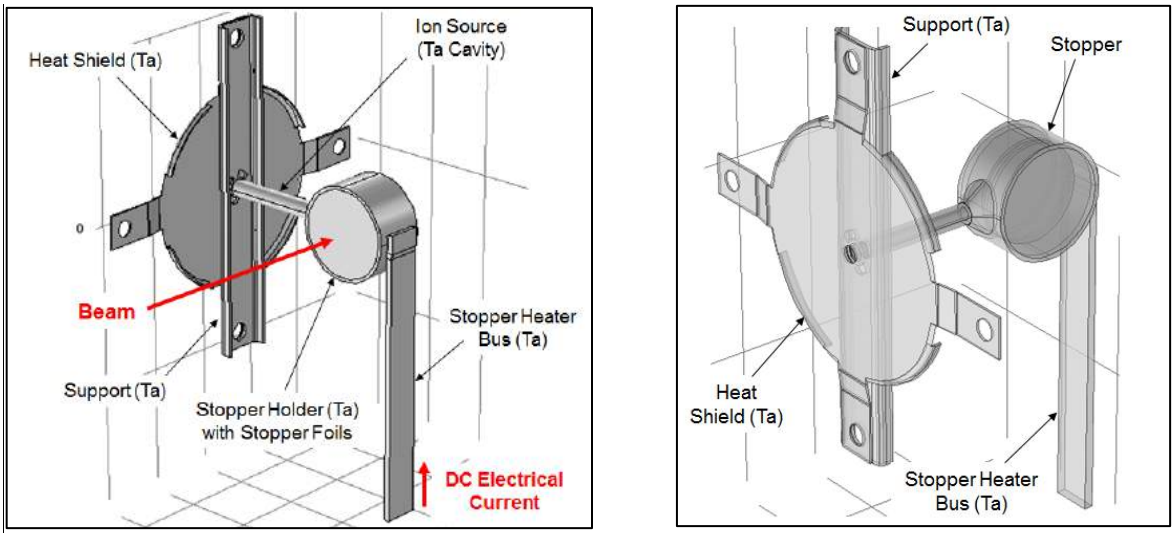

Figure 7-5. Two views of the 3D model of the POC stopper assembly with a Ta-cavity ion source and external resistive heating. The electrical current flows from the heater bus towards the stopper as indicated in the left diagram.

We again assume a fragment beam of ^{88}Sr ions with 187 MeV/u energy is incident on the system. The Sr ions are stopped, and the beam energy is completely deposited in the window and four stopper foils, as shown in Figures 6-2 and 6-3. The stopper holder and the ion source are resistively heated by DC electrical current which is applied to the stopper heater bus (Figure 7-5, left) and flows in series through the stopper holder, transfer tube, and ion source cavity. The heat shield and support of the ion source assembly are connected to the electrical ground via the mechanical support provided by screws inserted through the four screw holes shown in the diagram. For heat transfer simulations, the stopper system is assumed to be under vacuum, and hence heat conduction and surface-to-surface radiation are considered. The external surfaces of the stopper system are cooled by radiation to the ambient environment which is assumed to be at room temperature of 293.15 K. Further, the far end of the heater bus bar and the four screw holes of the ion source support and heat shield are fixed at a room temperature of 293.15 K.

Figure 7-6 shows the simulated temperature distribution of the stopper assembly with 400 A resistive heating and 10 nA of Sr beam stopped and depositing energy into the window and foils. Figure 7-7 presents the calculated temperature distributions in the four stopper foils for heating currents of 100 A and 400 A and input Sr beam intensities of 1 nA (Figure 7-7, left) and 10 nA (Figure 7-7, right). The maximum temperature of the foils as a function of the heating current is plotted in Figure 7-8.

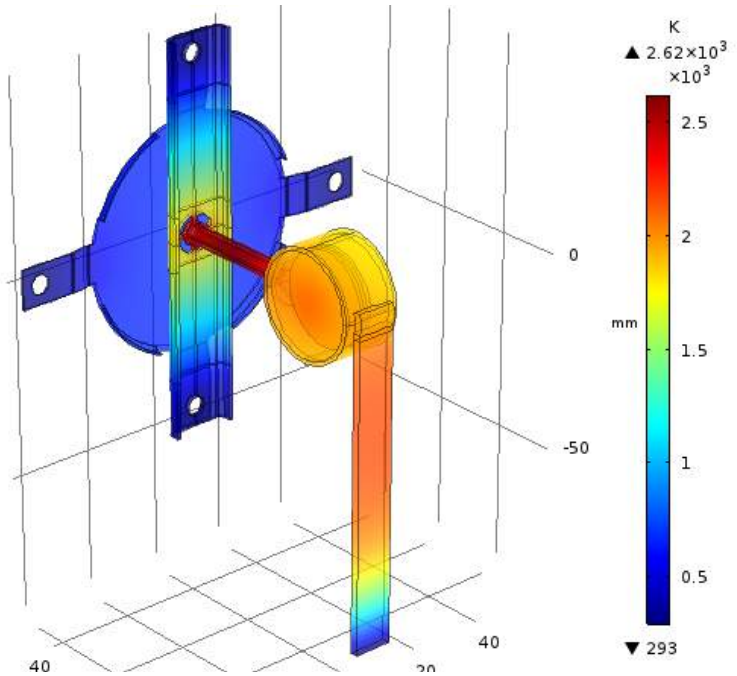

Figure 7-6. Temperature distribution of the stopper assembly stopping a 10 nA Sr beam and externally heated by 400 A electrical current.

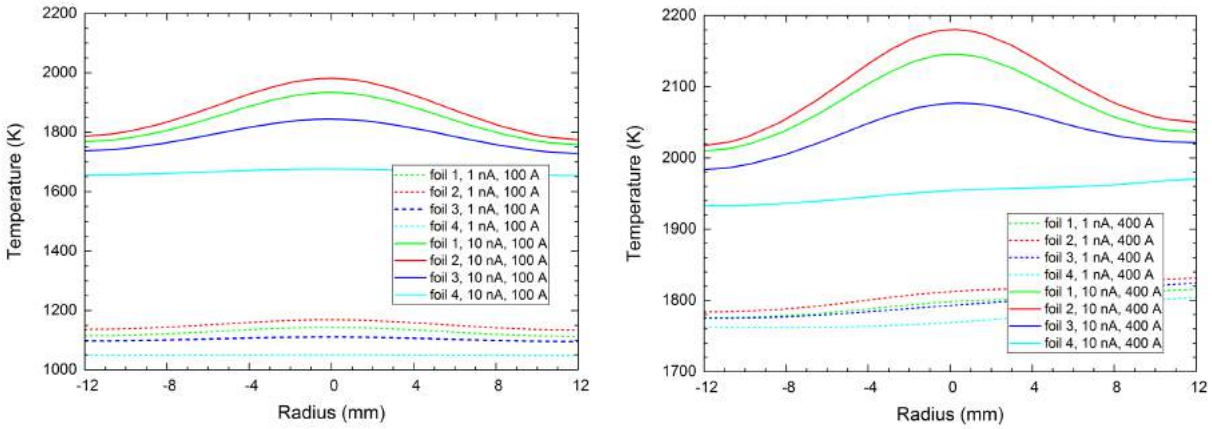

Figure 7-7. Temperature distribution of the stopper foils for Sr beams of 1 nA and 10 nA intensity, with external electrical heating current of 100 A (left) and 400 A (right).

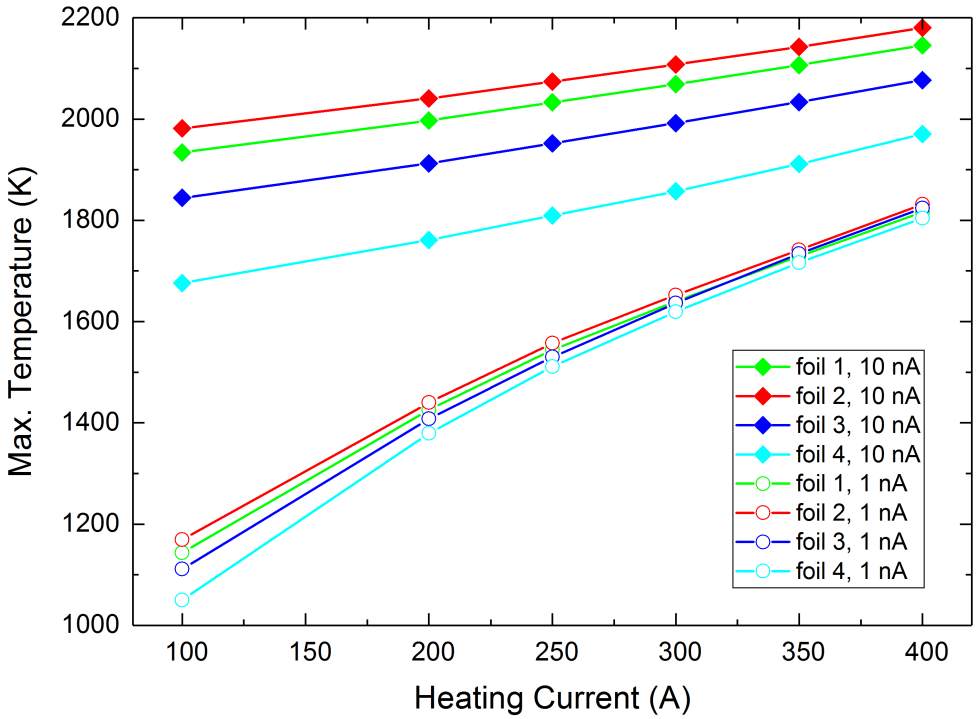

Figure 7-8. Maximum temperature of the stopper foils as a function of the external heating current, for 1 nA and 10 nA of stopped Sr beams.

Figure 7-9 shows the temperature distributions of the inner surfaces of the entrance window and the endcap at different heating currents. The maximum temperature of the window and endcap surfaces versus the heating current is given in Figure 7-10. The temperature distributions in the ion source cavity are shown in Figure 7-11.

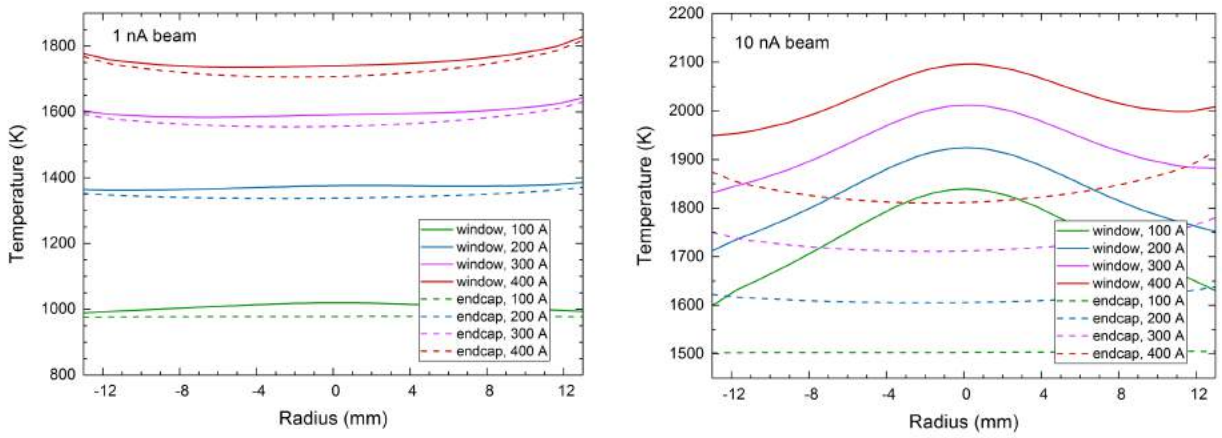

Figure 7-9. Temperature distribution of the inner surfaces of the window and the endcap at different external heating currents and for Sr beams of intensity 1 nA (left) and 10 nA (right).

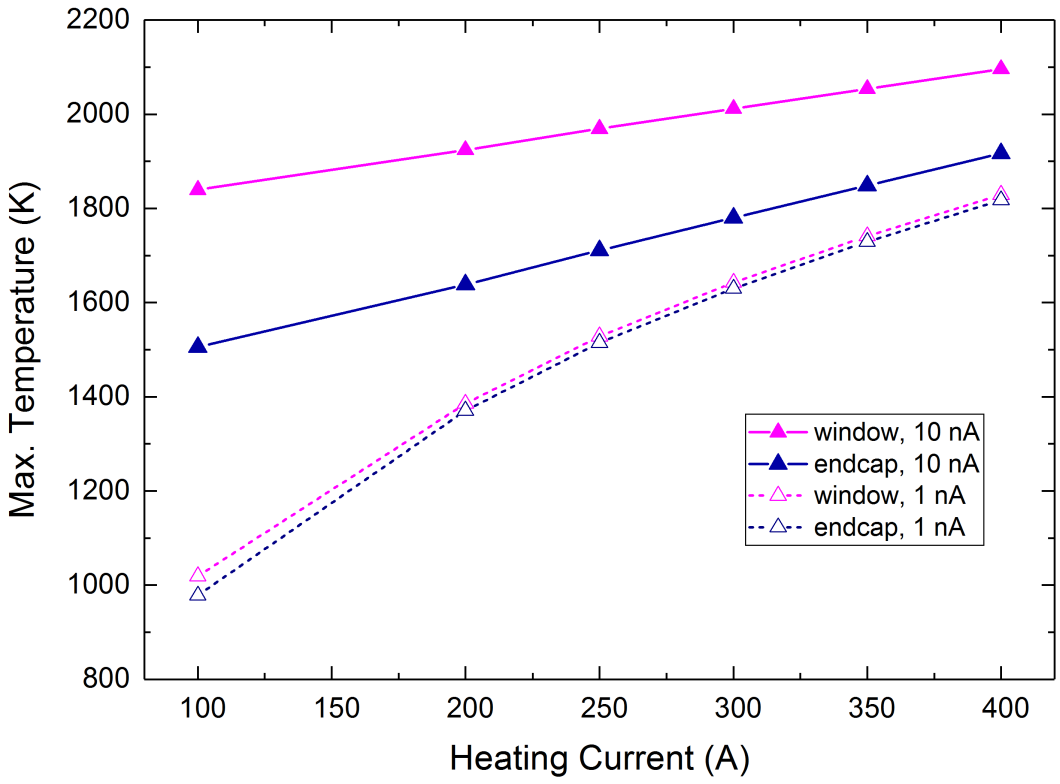

Figure 7-10. Maximum temperature of the window and endcap surfaces as a function of the external heating current for Sr beams of intensity 1 nA and 10 nA.

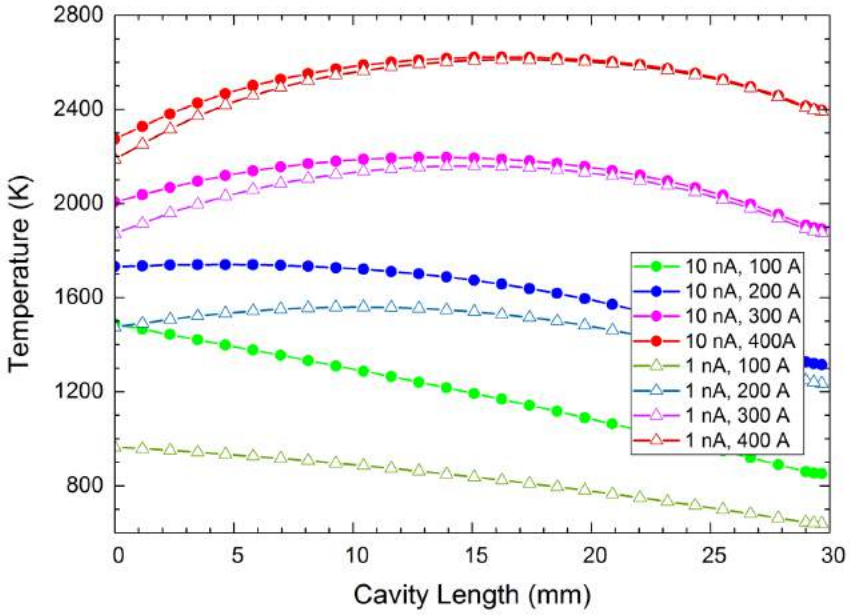

Figure 7-11. Inner surface temperature distribution of the ion source cavity at different external heating currents for Sr beams of intensity 1 nA and 10 nA.

These results indicate that the simple resistive heating scheme we employed can sufficiently heat the ion source and the stopper. In particular, the ion source cavity can be heated to above 2500 K with 400 A heating current. However, for Sr beam intensities equal to or less than 1 nA, the maximum temperature in the stopper is only about 1800 K (at 400 A heating) as shown in Figure 7-8. Since higher temperatures (> 2000 K) may be required for fast diffusion and effusion release, additional heating schemes must be considered. First, higher heating currents (> 400 A) could be used, but caution is needed to not melt the ion source cavity. Second, heat shields could be added to minimize the radiative heat loss from the stopper. Third, a radiative heating element could be added to heat the stopper holder. Fourth, an alternative heating configuration could be used, such as resistively heating the ion source cavity and radiatively heating the stopper. Some of these options will be investigated in future studies.

Coupled thermal-effusion simulations have been conducted to obtain the effusion times of Sr atoms released from the POC stopper system, with different external heating currents and under different surface sticking conditions. Again, the effusion simulations are conducted without the ion source, as shown in Figure 7-12. A total of 10000 Sr atoms are released at t = 0 from both surfaces of each of the four stopper foils, with a Gaussian spatial distribution on the foil surfaces and initial temperatures determined by the equilibrium temperature distributions of the foils resulting from both beam heating and the external resistive heating scheme described above. Figure 7-13 shows an example of the initial spatial and temperature distributions of the Sr atoms on the stopper foils before their release. The Sr atoms released from the foils are collected at the exit aperture and their characteristic effusion time t_c is calculated. Tables 7-2 and 7-3 give the t_c values

for 10 nA and 1 nA intensity incident Sr beams, respectively, with different external heating currents and different E_a values for surface sticking. As shown, external heating can reduce the effusion time by orders of magnitude, especially for a 1 nA beam intensity in cases where surface sticking is problematic.

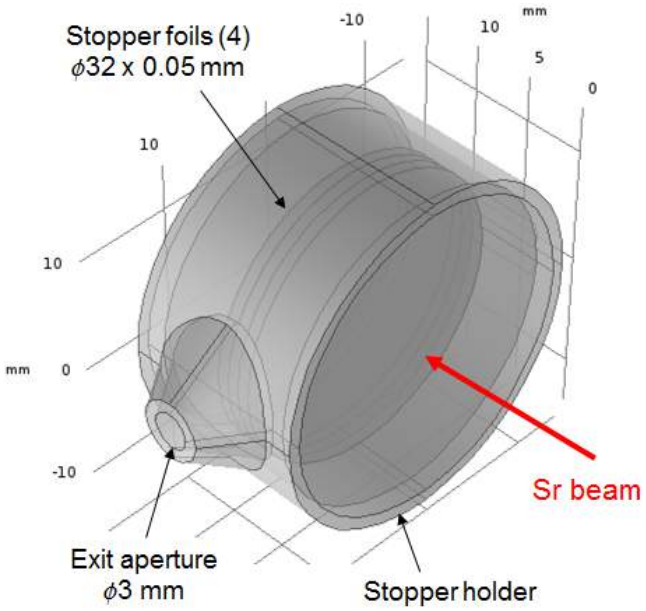

Figure 7-12. Effusion model for the coupled thermal-effusion simulation of the stopper assembly.

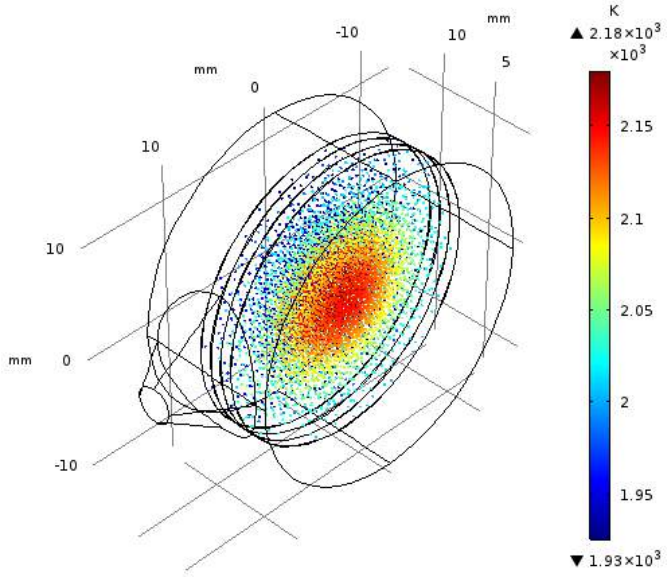

Figure 7-13. Initial spatial and temperature distributions of 10000 Sr atoms on the releasing surfaces of the foils. The stopper system is heated by Sr beam particles of intensity 10 nA and resistively heated by an external 400 A electrical current.

Table 7-2. Calculated effusion time t_c (s) for different activation energies of desorption E_a and external heating currents of 100 – 400 A for a 10 nA Sr beam.

E_a (eV)	100 A	200 A	300 A	400 A
0	0.0084(2)	0.0082(2)	0.0077(3)	0.0076(2)
0.25	0.0084(2)	0.0082(2)	0.0077(2)	0.0076(2)
1	0.0084(2)	0.0082(2)	0.0077(2)	0.0076(2)
2	0.0085(2)	0.0083(2)	0.0078(2)	0.0077(2)
3	0.225(3)	0.061(1)	0.023(1)	0.013(2)
4	407(7)	57(2)	10.2(2)	2.6(1)
5	8.12E+05	66645	7570(190)	1298(44)

Table 7-3. Calculated effusion time t_c (s) for different activation energies of desorption E_a and external heating currents of 100 A – 400 A for a 1 nA Sr beam.

E_a (eV)	100 A	200 A	300 A	400 A
0	0.011(1)	0.009(1)	0.0084(2)	0.0081(2)
0.25	0.011(1)	0.009(1)	0.0084(2)	0.0081(2)
1	0.011(1)	0.009(1)	0.0084(2)	0.0081(2)
2	0.65(1)	0.011(1)	0.0085(2)	0.0082(2)
3	77857	7.82(5)	0.23(1)	0.039(1)
4	9.97E+09	39043(410)	334(2)	24.7(1)
5	1.31E+15	1.99E+08	5.15E+05	19820(50)

8. INTEGRATING MODELS AND TOOLS TO FORM AN END-TO-END SYSTEM DESIGN WORKFLOW

The tools and methods described above are the components of a work flow for studies of solid stopper systems that includes material evaluation, ion implantation simulation, thermal analysis of limiting temperatures including beam heating and external heating, and estimation of diffusion and effusion release rates at the expected operating temperatures including surface sticking effects. This workflow facilitates the systematic investigation of a wide variety of different system designs. As mentioned in Section 2, the codes used in this workflow are: HSC Chemistry to evaluate and select potential stopper materials; LISE++ to simulate the fragment stopping depth profiles and beam power deposition distributions in the stopper materials; COMSOL Multiphysics with its Heat Transfer Module to simulate system heating via heavy-ion bombardment and external heaters; COMSOL Multiphysics [with its Particle Tracing Module to simulate the effusion of neutral species from the stopper material to the ion source; and analytical solutions of Fick's equations for diffusion of neutrals out of the stopper foils. The use of the COMSOL Multiphysics software

platform enabled the integration of the thermal and effusion simulations, and in future studies will be used for diffusion as well.

9. CONCLUSION

This report details the R&D effort at ORNL to develop a solid stopper system to generate reaccelerated beams of unstable nuclei at FRIB. We have developed an end-to-end computational workflow for systematic investigation of solid stopper design options using HSC Chemistry, LISE++, and COMSOL software packages. We have developed coupled thermal-effusion simulation models using the COMSOL Multiphysics software package that enables us to include the effects of beam heating and external heating in the stopper system, effusive transport of stopped fragment species to an ion source, and surface sticking. The diffusion delay time is calculated analytically and combined with the effusion delay time by convolution.

A set of suitable candidate stopper materials (including C, Ta, W, Mo, and Nb) have been selected based on their known capabilities of handling the high temperatures resulting from ion beam bombardment. We also chose to focus on stopping unstable heavy ions that are alkali, alkaline earth, and noble gas elements, based on the high production yields expected at FRIB for these species.

We investigated various stopper geometries and vapor transport configurations for fast effusive release, including the target and ion source systems used at different Isotope Separator Online (ISOL) facilities as well as over 20 new custom solid stopper configurations. These studies show that the particle effusion time in a stopper system is (1) determined by the effusion volume (*i.e.*, the volume of the stopper chamber) and the conductance of the stopper and vapor transport system, (2) decreases with increasing temperature, and (3) decreases with increasing number of stopper disks. We also found that the average number of surface collisions per particle increases with the number of stopper disks. If the surface sticking time is not trivial, the total delay time (effusion + surface sticking) can be significantly longer with additional stopper disks. For fastest release, we conclude that the solid stopper system should use as few stopper disks as possible, have a small total volume, have a high molecular conductance, and operate at high temperatures. For the cases in which beam heating is insufficient to adequately raise the system temperature, external heating can be employed to significantly reduce the effusion time, by orders of magnitude in cases where surface sticking is significant. We also demonstrated that simulations that couple thermal properties and particle effusion can give more realistic effusion delays than non-coupled effusion simulations.

We developed a proof-of-concept design for a solid stopper system that can efficiently release ions for reaccelerated beam experiments. As a benchmark case, stopping of fast 187 MeV/u Sr beams was

simulated, in which the fast Sr ions were first slowed by 1.65 mm Ta window and then completely stopped in four Ta stopping foils of 50 μm thickness. With an incident Sr ion beam of 10 nA intensity, the stopper foils were heated to temperatures ranging from 1650 K to 2000 K and the characteristic effusion time for Sr atoms were calculated to be less than 10 ms without surface sticking. We anticipate optimizing this design for eventual construction, installation, commissioning, and utilization to generate reaccelerated unstable beams at FRIB.

REFERENCES

1. C. Wrede, "The Facility for Rare Isotope Beams," EPJ Web of Conferences **93**, 07001 (2015).
2. W.R. Plaß, et al., "The FRS Ion Catcher – A facility for high-precision experiments with stopped projectile and fission fragments," Nucl. Instr. Meth. **B 317**, 457 (2013).
3. S. Schwarz, et al., "The NSCL cyclotron gas stopper – Under construction," Nucl. Instr. Meth. **B 317**, 463 (2013).
4. G. Bollen, "Beam Development," Separator for Capture Reactions SECAR Collaboration Meeting, Aug. 20, 2015, Michigan State University, East Lansing, MI.
5. M. Lindroos, "Review of ISOL-type Radioactive Beam Facilities," Proceedings of EPAC 2004, p. 45 (2004).
6. https://www.ansys.com/.
7. https://www.comsol.com.
8. Y. Zhang, G.D. Alton, Nucl. Instr. Meth. **A 521** (2004) 72-107.
9. Y. Zhang, I. Remec, G.D. Alton, Z. Liu, Nucl. Instr. Meth. **A 620** (2010) 142–146.
10. L. Egoriti, S. Boeckx, L. Ghys, D. Houngbo, L. Popescu, Nucl. Instr. Meth. **A 832** (2016) 202–207.
11. M.S. Leitner, "A Monte Carlo code to optimize the production of radioactive ion beams by the ISOL technique," Ph.D. thesis, Technical University of Catalonia (UPC), 2005.
12. Y. Zhang, G.D. Alton, J. Vac. Sci. Technol. **A 23** (2005) 1558-1567.
13. B. Mustapha, J.A. Nolen, Nucl. Instr. Meth. **B 204** (2003) 286-292.
14. R. Kersevan, J.L. Pons, J. Vac. Sci. Technol. **A 27** (2009) 1017-1023.
15. J.C. Bilheux, "Design studies of high-power fast diffusion-release targets and fast vapor-transport system for radioactive ion beams," Ph.D. thesis, Universitè de Versailles, Saint-Quentin-en-Yvelines, 2003.
16. http://www.outotec.com/en/Products--services/HSC-Chemistry/
17. http://www.srim.org/
18. http://lise.nscl.msu.edu/lise.html
19. G. Bollen, private communication.
20. https://groups.nscl.msu.edu/frib/rates/fribrates.html
21. K. Frisk and A. Ferndndez Guillermet, Journal of Alloys and Compounds 238 (1996) 167-179.

22. J. Cruz Fernandes et al., Solar Energy 80 (2006) 1553–1560.

23. Haase V. et al. (1985) The Si-C Phase Diagram. In: Katscher H., Sangster R., Schröder F. (eds) Si Silicon. Gmelin Handbook of Inorganic Chemistry / Gmelin Handbuch der Anorganischen Chemie, vol S-i / B / 1-5 / 3. Springer, Berlin, Heidelberg.

24. M. Knudsen, *The cosine law in the kinetic theory of gases* (National Aeronautics and Space Administration, Washington, D.C. 1967).

25. P. Clausing, J. Vac. Sci. Technol. **8** (1971) 636-646.

26. D. J. Santeler, J. Vac. Sci. Technol. **A 4** (1986) 338-343.

27. A. Mohan, R.V. Tompson, S.K. Loyalka, J. Vac. Sci. Technol. **A 25** (2007) 758-762.

28. A. S. Berman, J. Applied Phys. **40** (1969) 4991-4992.

29. G.D. Alton, J.-C. Bilheux, Y. Zhang, Y. Liu, Nucl. Instr. Meth. **B 329** (2014) 30-39.

30. B. Mustapha, J.A. Nolen, Nucl. Instr. Meth. **A 521** (2004) 59–64.

31. H. Weick et al., Nucl. Instr. and Meth. in Phys. Res. B 164-165 (2000) 168-179.

32. D. J. Morrissey and B. M. Sherrill, *In-Flight Separation of Projectile Fragments*, Lect. Notes Phys. 651 (2004) 113-135.

33. R. Kirchner, Nucl. Instr. Meth. **B 70** (1992) 186-199.